32

# Cardiac Myocardial Disease States Cause Left Ventricular Remodeling with Decreased Contractility and Lead to Heart Failure; Interventions by Coronary Arterial Bypass Grafting and Surgical Ventricular Restoration Can Reverse LV Remodeling with Improved Contractility

Dhanjoo N. Ghista[1], Liang Zhong[2], Leok Poh Chua[3], Ghassan S. Kassab[4], Yi Su[5] and Ru San Tan[2]
[1]*Department of Graduate and Continuing Education, Framingham State University, Framingham, Massachusetts,*
[2]*Department of Cardiology, National Heart Centre,*
[3]*School of Mechanical and Aerospace Engineering, Nanyang Technological University,*
[4]*Departments of Biomedical Engineering, Surgery, Cellular and Integrative Physiology, Indiana University-Purdue University Indianapolis, Indianapolis, Indiana,*
[5]*Institute of High Performance Computing, Agency for Science, Technology and Research,*
[1,4]*USA*
[2,3,5]*Singapore*

## 1. Introduction

### 1.1 Theme and scope

In this chapter, we are studying the course (i) of cardiomyopathy diseased LVs (with myocardial infarcts) progressing to heart failure (HF) through LV remodelling and decreased LV contractility, and (ii) their recovery through surgical therapeutic interventions of CABG and Surgical Ventricular Restoration (SVR), by restoration of myocardial ischemic segments, reversal of LV remodeling and improvement in LV contractility.

For this purpose, we first provide the methodology for detecting myocardial infarcts. Then, we characterize LV remodeling of cardiomyopathy diseased LVs (with myocardial infarcts) in terms of reduced change in curvedness from end-diastole to end-systole. In these LVs, there is also reduced contractility; so we provide an index for cardiac contractility, in terms of maximal rate-of-change of normalized wall stress, $d\sigma^*/dt_{max}$, and its decrease in an infarcted LV progressing to heart failure. We provide clinical studies of remodeled cardiomyopathy diseased LVs, in terms of reduced values of their curvedness index and contractility index.

By way of therapeutic interventions, we have presented the hemodynamic flow simulation of the CABG (carried out to enhance myocardial perfusion in the region around the blocked coronary artery), and pointed out certain factors and sites of wall shear stresses that cause intimal damage of vessels and hyperplasia, as potential causes for decreased patency. We

have shown that surgical ventricular restoration (SVR), in conjunction with CABG, is seen to benefit the ischemic-infarcted heart, by (i) restoration of cardiac remodeling index of 'end-diastolic to end-systolic curvedness change', (ii) reduction of regional wall stresses, and (iii) augmentation of the cardiac contractility index value.

## 2. Myocardial infarction: What it entails

In Cardiology, the etiology of congestive heart failure (CHF) is coronary artery disease in approximately two-thirds of cases. The majority of these patients have hearts with myocardial infarcted segments. This infarcted myocardial wall mitigates adequate contraction of the wall. So, the end-result of an infarcted left ventricle (LV) is poor intra-LV velocity distribution and pressure-gradient distribution, causing impaired outflow from the LV into the aorta.

In the infarcted myocardial segments, the myocardial infrastructure of actin and myosin filaments (and their cross – bridges) is disrupted, and hence there is no contraction within these infarcted myocardial segments. The below figure 1 illustrates a myocardial sarcomere segment's bioengineering model, composed of two symmetrical myocardial structural units (MSUs). In these MSU(s), the contractile elements represent the actin-myosin contractile components of the sarcomere segment. The disruptions of these contractile elements impair the contractile capability of that sarcomere segment. Hence, a LV with infarcted myocardial segments will have diminished contractility, inadequate and improper intra-LV flow, and poor ejection.

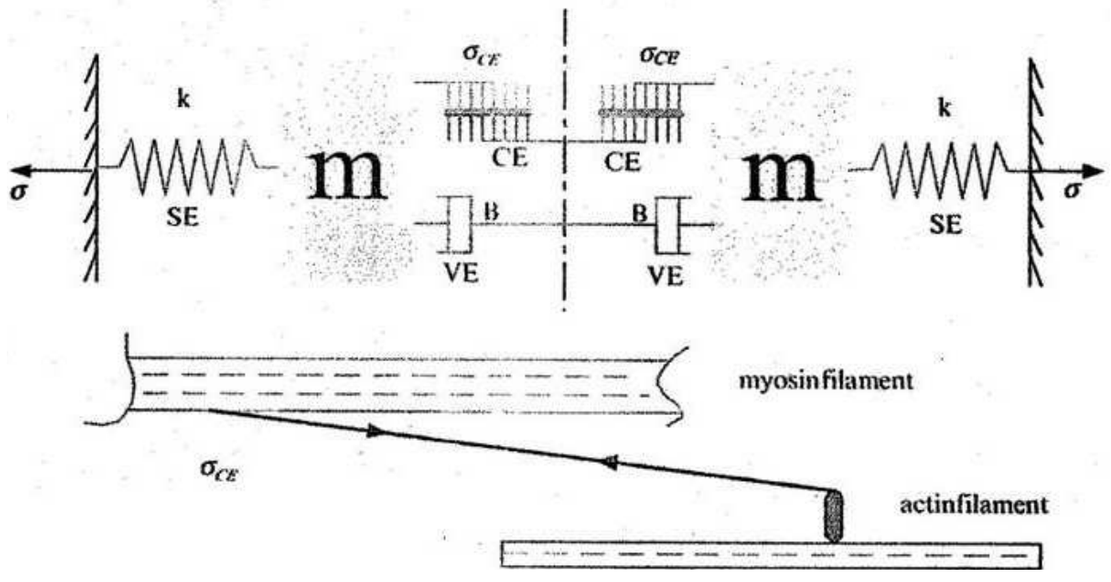


Fig. 1. Based on the conventional Hill three-element model and Huxley cross bridge theory, we have developed a myocardial model involving the LV myocardial mass, series-elastic element (CE),. In this figure we have linked the anatomical associations of these myocardial model elements with microscopic structure of the heart muscle. This figure illustrates the sarcomere element contractile model, involving: the effective mass ($m$) of the muscle tissue that is accelerated: elastic parameter k of the series element stress $\sigma_{SE}$ (k = elastic modulus of the sarcomere), viscous damping parameter B of the stress $\sigma_{VE}$ in the parallel viscous element VE, the generated contractile stress $\sigma_{CE}$ between myosin (thick ) and actin (thin ) filaments.

## 3. Detection of myocardial infarcted segments

Now, infarcted myocardial segments can be detected as highly reflectile echo zones (HREZs) in 2-dimensional B-scan echocardiograms. In this context, we have shown how infarcted myocardial segments can be detected (in shape and size), by echo-texture analysis, as highly reflectile echo zones or HREZs. Each myocardial tissue component of the heart generates a grey scale pattern or texture related to the tissue density and fibrous content. In diseased states (such as myocardial ischemia, myocardial fibrosis, and infiltrative diseases), changes in myocardial tissue density have been recognised by employing echo intensity and mean grey level of pixel as the basis for recognition of such myocardial disorders. It is found that hyper-reflectile echoes (HREs) correlated well with diseased cardiac muscle, and that myocardial tissue containing HREs corresponded with foci of sub-endorcardial necrosis and even calcification.

In our study [1], in order to determine highly reflectile echo zones (HREZs), echocardiograms were recorded, and each image was made up of 256 x 256 pixels, with each pixel having a resolution of 0-256 grey scales. The echocardiographic images were digitised into 256 grey scales. Then, echo intensity levels from normal infants were used to delineate the range of echo intensities for normal tissues. The upper bound of the echo intensity was set to 100 per cent in each normal infant, and the intensities from the rest of the image were referenced to this level. Normally, pericardium had the highest intensity level. It was found that the upper-bound of the echo intensity value for healthy tissue (expressed as a percentage of the pericardial echo intensity value) was 54.2.

| Patient (Sex) | Region A | Region B | Region C | Region D | HRE and its location |
|---|---|---|---|---|---|
| B | M: 167.44 | 54.76 | 51.02 | 82.20 | 105.74 |
| (M) | SD: 25.00 | 28.2 | 17.71 | 24.68 | 30.88 |
| | N: 65 | 84 | 75 | 31 | 65 |
| | P: 100 | 32.7 | 30.5 | 49.1 | 63.1 |
| | | | | | Septum |
| P | 148.76 | 61.73 | 79.81 | 61.7 | 108.18 |
| (F) | 26.78 | 23.02 | 22.05 | 24.2 | 13.03 |
| | 50 | 75 | 47 | 49 | 40 |
| | 100 | 41.5 | 53.8 | 41.5 | 72.6 |
| | | | | | Septum |
| Br | 141.65 | 68.3 | 69.3 | 33.93 | 89.412 |
| (M) | 29.56 | 26.8 | 24.8 | 24.4 | 28.0 |
| | 40 | 40 | 49 | 44 | 79 |
| | 100 | 41.5 | 53.8 | 41.5 | 73.1 |
| | | | | | Septum |
| F | 157.34 | 50.1 | 60.8 | 53.8 | 112.1 |
| (F) | 30.0 | 29.5 | 18.8 | 22.7 | 10.3 |
| | 35 | 45 | 49 | 44 | 31 |
| | 100 | 31.8 | 38.6 | 34.2 | 71.2 |
| | | | | | R. ventricle |
| HI | 168.1 | 54.7 | 58.2 | 62.4 | 96.4 |
| (M) | 21.35 | 21.8 | 16.9 | 20.0 | 14.7 |
| | 47 | 36 | 35 | 37 | 49 |
| | 100 | 32.5 | 34.6 | 37.1 | 57.3 |
| | | | | | L. ventricle |
| G | 117.7 | 46.9 | 45.5 | 42.7 | 85.3 |
| (M) | 20.6 | 19.0 | 20.6 | 19.1 | 22.6 |
| | 45 | 44 | 40 | 49 | 37 |
| | 100 | 39.8 | 38.7 | 36.2 | 72.5 |
| | | | | | R. ventricle |

A = Posterior Pericardium, B = Anterior Myocardium, C = Posterior Myocardium, D = Septum

Table 1. Echo intensity values for various anatomic regions of diseased pediatric hearts (based on long axis view). The numbers in the four rows represent Mean (M), Standard Deviation (SD), Number of Pixels (N), Percentage of Posterior Pericardial Intensity (P). This figure is adopted from Ref [1].

For patients whose echo-texture analysis showed presence of HREs, it was found that the echocardiographic intensities of the HREs from these patients intensities were distinctly higher than the echo intensity range of normal tissue (as depicted in Table 1).
Myocardial tissue pixels having echo-intensity values greater than 200 are generally noted to be infarcted. This region's echo-intensity values can remain unaffected by administration of a myocardial perfusing agent. This infarcted sub-region is seen to be surrounded by an ischemic sub-region whose pixels are noted to have echo intensity values between 100 and 200. This region's echo-intensity can be reduced by the administration of a myocardial perfusing agent. The surrounding healthy tissue has echo intensity less than 100. Figure 2(a) depicts an echo image of an infant with visible scars regions 1 and 2, while figure 2(b) depicts printouts of the echo intensities from these two regions, wherein the infarcted segments are depicted in dark colour and the surrounding ischemic segments are depicted in a lighter shade.

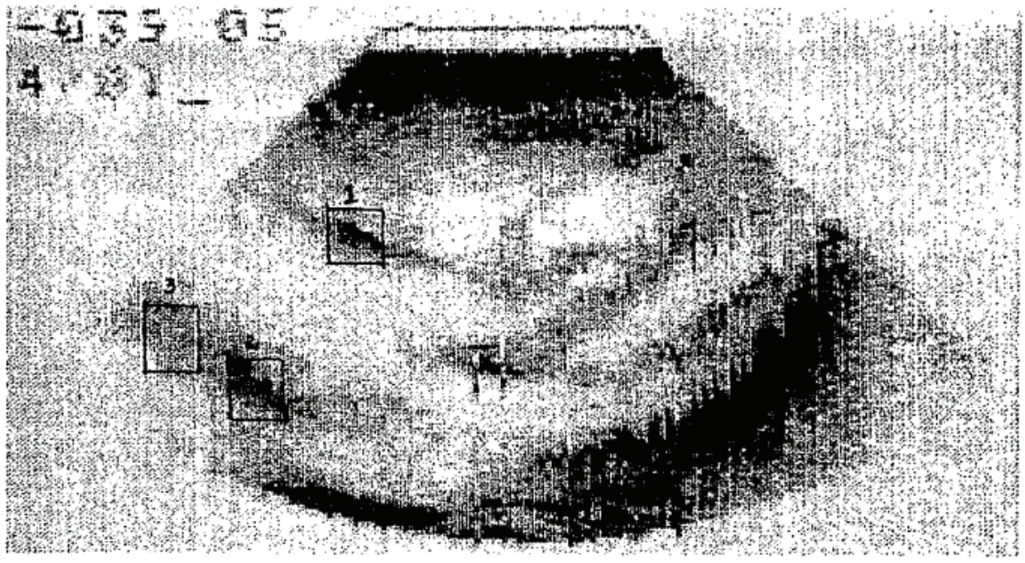


Fig. 2. (a) Long axis view of a pediatric patient's heart showing HRE regions 1 and 2 and a healthy region 3 [1].

| Y/X | 99 | 100 | 101 | 102 | 103 | 104 | 105 | 106 | 107 | 108 | 109 | 110 | 111 | 112 | 113 | 114 |
|---|---|---|---|---|---|---|---|---|---|---|---|---|---|---|---|---|
| 98 | 79 | 78 | 88 | 90 | 99 | 96 | 102 | 108 | 91 | 77 | 92 | 86 | 135 | 122 | 73 | 55 |
| 99 | 114 | 115 | 101 | 114 | 126 | 128 | 114 | 116 | 119 | 126 | 82 | 68 | 84 | 103 | 78 | 57 |
| 100 | 151 | 137 | 125 | 128 | 136 | 135 | 133 | 134 | 149 | 137 | 91 | 75 | 74 | 73 | 82 | 83 |
| 101 | 175 | 177 | 171 | 151 | 144 | 143 | 154 | 147 | 138 | 142 | 139 | 139 | 126 | 64 | 76 | 71 |
| 102 | 202 | 196 | 174 | 125 | 192 | 193 | 183 | 164 | 131 | 131 | 125 | 132 | 92 | 89 | 81 | 116 |
| 103 | 139 | 143 | 183 | 193 | 206 | 217 | 233 | 248 | 209 | 146 | 116 | 102 | 111 | 113 | 117 | 116 |
| 104 | 147 | 136 | 143 | 178 | 203 | 251 | 250 | 255 | 229 | 201 | 75 | 71 | 92 | 82 | 88 | 95 |
| 105 | 108 | 110 | 132 | 151 | 210 | 223 | 227 | 249 | 255 | 255 | 230 | 210 | 104 | 87 | 81 | 112 |
| 106 | 84 | 104 | 88 | 121 | 147 | 184 | 227 | 239 | 255 | 255 | 252 | 247 | 220 | 125 | 76 | 70 |
| 107 | 83 | 110 | 108 | 122 | 135 | 175 | 194 | 183 | 206 | 228 | 211 | 255 | 255 | 184 | 141 | 131 |
| 108 | 68 | 92 | 122 | 131 | 145 | 147 | 149 | 151 | 217 | 181 | 189 | 222 | 241 | 178 | 190 | 167 |
| 109 | 56 | 76 | 81 | 122 | 132 | 137 | 145 | 143 | 154 | 150 | 156 | 156 | 195 | 190 | 206 | 190 |
| 110 | 76 | 63 | 96 | 96 | 82 | 83 | 103 | 120 | 142 | 128 | 133 | 141 | 153 | 181 | 192 | 194 |
| 111 | 59 | 57 | 63 | 66 | 70 | 103 | 106 | 118 | 96 | 94 | 86 | 110 | 129 | 150 | 96 | 66 |
| 112 | 58 | 60 | 59 | 57 | 58 | 61 | 71 | 77 | 106 | 89 | 91 | 92 | 100 | 147 | 97 | 85 |
| 113 | 74 | 71 | 78 | 60 | 56 | 58 | 57 | 62 | 71 | 70 | 79 | 83 | 78 | 92 | 67 | 76 |
| 114 | 57 | 57 | 65 | 63 | 57 | 56 | 63 | 56 | 51 | 56 | 58 | 80 | 85 | 78 | 67 | 55 |
| 115 | 51 | 60 | 63 | 63 | 58 | 67 | 56 | 57 | 54 | 59 | 57 | 58 | 59 | 76 | 68 | 81 |

Fig. 2. (b) Pixel values correcponding to highly reflectile echo region 1. The central region having echo-intensity values greater than 200 is infarcted, while its immediately surrounding region shown in lighter shade is ischemic.

In this way, in each highly reflectile echo zone (HREZ) made up of , say, N number of pixels, we can determine the number (I) of infarcted pixels. The ratio I/N represents the infarcted potion of that HREZ myocardial segment. The total number of all the infarcted pixels in all the HREZs provides an indication of the amount of infarcted myocardium of the heart or of the LV.

## 4. Cardiac remodeling following myocardial infarction and progression to heart failure

Myocardial infarction (MI) reduces the amount of ventricular contractile myocardium, which in turn reduces the left ventricular (LV) contractile capacity for pumping out adequate cardiac output (CO). As MI extends, it progresses into heart failure (HF). A manifestation of MI and its decreased contractile capacity is the inability of the LV to retain its compact systolic curved shape. In other words, in HF resulting from MI, the left ventricle undergoes remodeling and its curvedness index decreases. As MI progresses into HF, LV size increases, LV function deteriorates, and symptoms of HF become evident. Thus, cardiac remodeling (expressed in terms of regional curvedness of the LV) constitutes a measure of the progression of HF after MI, and interventions causing some reversal of this LV remodeling process have been shown to improve mortality in patients with HF. Therefore, reversal of LV remodeling (through medical or surgical treatment) has been emerging as a therapeutic target in HF of all etiologies. The challenge is to develop specific measures of LV remodeling that can be incorporated into the clinical management pathway. For patients with HF after MI, the LV shape is more spherical in terms of the global sphericity index. However, focus on global sphericity index may be misleading, since the simple plane ratio reflects a linear alteration in the two axes of the LV chamber. Hence, regional curvedness index, determined from 3D magnetic resonance imaging (MRI)-based LV model, is proposed as a measure of LV shape. The curvedness value describes the magnitude of the curvature at a surface point, i.e., a measure of degree of curvature a point; the regional curvedness describes the curvedness of the segment of the LV. In MI patients, the regional curvedness index value does not increase significantly from end-diastole to end-systole (due to decreased LV contractile capacity), as in the case of normal patients.

In the case of patients with HF following MI, the LV cannot generate adequate contractile force, as explained earlier in section 1. As a result, the overall LV contractility index of maximal rate-of-change of normalized systolic wall stress $d\sigma^*/dt_{max}$ is decreased, and the LV ejection force is also diminished. Now, LV regional wall stress is proportional to the wall surface radius-of-curvature and inversely proportional to the wall thickness. Hence, for patients with HF after MI, the inability of the remaining viable myocardium to compensate for the increased wall stress associated with LV dilatation and thinning is a trigger for LV enlargement.

### 4.1 Remodeling quantification in terms of local curvedness indices and regional curvedness index

#### 4.1.1 Overall approach

The remodeling is characterized in terms of the *Regional Curvedness* index of the 16 segments of the LV endocardial surface. The method entails generation of the LV endocardial shape and its compartmentalization into 16 segments or regions (as explained later on). Each segment is discretized into triangular meshes, so that a point on the endocardial surface is a vertex of a triangular mesh. At each vertex point, we determine the *Local Curvedness* index

[2], by employing its surrounding neighboring vertices in the form of *n*-rings around the local point. To ensure accurate curvedness computation without over smoothing, the optimal number of *n*-rings is determined to be 5. Then, for each segment, we determine the *Regional Curvedness* index, as the mean of the *Local Curvedness* indices in the segment.
The values of *Regional Curvedness* are determined for normal and MI patients, at end-diastolic and end-systolic instants. For normal patients, the *Regional Curvedness* index changes significantly from diastole to systole, as given by the *Diastole-to-Systole Change in Curvedness* (%ΔC) [2]

$$\%\Delta C = \frac{C_{ED} - C_{ES}}{C_{ED}} \times 100 \tag{1}$$

wherein $C_{ED}$ and $C_{ES}$ are end-diastolic and end-systolic curvedness, defined later on. The mean alteration in regional curvedness index value of %ΔC is determined for all the segments, for normal subjects and MI patients (and logged in Table 3). It can be seen that for MI patients, the regional curvedness index or (%ΔC) does not change significantly from end-diastole to end-systole, in comparison with normal subjects.

### 4.1.2 Clinical application methodology

Our study involved 10 normal subjects and 11 patients after myocardial infarction (MI). The hemodynamic and volumetric parameters of the subjects are summarized in Table 2.
*Human Subjects and MRI Scans*: The study to characterize regional curvedness index or (%ΔC) involved ten normal subjects and 11 patients after myocardial infarction [2]. All subjects underwent diagnostic MRI scans. For each subject, short-axis MRI images were taken along the plane which passes through the mitral and aortic valves of the heart at an interval of 8mm thickness. Each image has a spatial resolution of 1.5mm, acquired in a single breath hold, with 25 temporal phases per heart cycle. Of these images, the set of images corresponding to the cardiac cycle at end-diastole and end-systole are then used for the study.
*LV Endocardial Surface Reconstruction and Segmentation:* The MRI images were processed, by using a semi-automatic technique that is included in the CMRtools suite (Cardiovascular Solution, UK). The contours demarcating the myocardium and the LV chamber were defined by means of B-spline curves. The endocardial surface of the LV was reconstructed by joining the series of contours to form a triangle mesh. In order to facilitate quantification of the LV segmental regional curvedness, the endocardial surface was partitioned into 16 segments; the method of segmentation of the LV endocardial surface is provided in our paper [2].
*Left Ventricular Shape Analysis:* To quantify LV remodeling, we first define a measure known as the *Local Curvedness* index [2]. This is essentially a shape descriptor used to quantify how curved the surface is in the vicinity of a vertex on the LV endocardial surface. This is done by using the 3-d mesh of the LV endocardial surface as an input. Each vertex of the mesh is processed by fitting a quadric surface over a local region around the vertex as described in our paper [2]. The extent of this local region is determined by the *n*-ring parameter. Next, the *Local Curvedness* index of each vertex can be calculated from the coefficients of the fitted quadric surface by [2]:

$$C = \sqrt{\frac{\kappa_1^{\,2} + \kappa_2^{\,2}}{2}} = \frac{1}{A^2}\sqrt{\frac{2B^2 + A^2\left(4ac - b^2\right)}{A}} \tag{2}$$

such that

$$A = \sqrt{d^2 + e^2 + 1}$$

$$B = a + ae^2 + c + cd^2 + bde$$

where *a*, *b*, *c*, *d* and *e* are the coefficients of the fitted quadric surface at the vertex.
In order to derive the *Regional Curvedness*, the endocardial surface is partitioned into 16 segments (Fig 3). The *Regional Curvedness* for the each segment is the mean of the *Local Curvedness* indices in the segment. The flowchart of the overall workflow for the regional LV shape analysis is shown in Fig. 4.

### 4.1.3 Clinical studies results

In our clinical studies, it was found that (1) MI patients exhibit decreased curvedness and %Δ*C*, (2) MI patients exhibit increased variation of curvedness and variation of %Δ*C*, and (3) LV ejection fraction is positively correlated with curvedness and %Δ*C*, and inversely correlated with variation of %Δ*C*.
The *Diastole-to-Systole Change in Curvedness* (%Δ*C*), as defined by equation (1), is a measure of regional deformity due to contraction. Positive values of %Δ*C* indicate regions of increasing inward concavity of the LV wall during systole, while negative values of %Δ*C* indicate wall regions of decreasing inward concavity. The %Δ*C* measure can be employed to relate the regional differences in hypokinesis due to myocardial infarction.
*Variation of curvedness:* The extent of LV surface inhomogeneity is characterized by a coefficient of variation of curvedness at end-diastole (CV_$C_{ED}$) and end-systole (CV_$C_{ES}$):

$$CV\_C = \frac{\sigma(C)}{\mu(C)} \tag{3}$$

where $\sigma(C)$ is the standard deviation of the regional curvedness and $\mu(C)$ is the mean of the regional curvedness of the segments of the LV mesh.
To evaluate the extent of functional non-uniformity of LV regions, the index CV_DC was determined as [2]:

$$CV\_\Delta C = \frac{CV\_C_{ED} - CV\_C_{ES}}{CV\_C_{ED}} \times 100 \tag{4}$$

In general, the larger the values of CV_$C_{ED}$ and CV_$C_{ES}$, the more inhomogeneous the LV endocardial surface appears. Hence, the larger the value of index CV_Δ*C*, the more functionally non-uniform are the LV shape changes due to LV contraction.
*Curvedness, Variation of curvedness and Diastole-to-systole change %Δ C in MI patients compared to Normal subjects:* The hemodynamic and volumetric parameters of the subjects are summarized in Table 2. For patients after MI, the LV ejection fraction was significantly lower than that in the control subjects. In addition, their LV end-diastolic and end-systolic indexed volumes were greater than those in the control subjects.
The values of regional curvedness from apex to base in MI patients and normal subjects are given in Table 3 and Fig. 5, to highlight the regional variations of the LV curvature. In the normal group, there was a significant increase in the curvedness at the apex from diastole to systole. However, in MI patients, there was no significant difference in curvedness in all

segments. Significant differences in end-diastolic curvedness $C_{ED}$ and end-systolic curvedness $C_{ES}$ were noted between MI and normal groups. Among the 16 segments of the LV, the variation coefficient of $C_{ES}$ (CV_$C_{ES}$) was significantly lower in MI patients than in the normal group (18±4% in MI vs 31±8% in normal, $p<0.0001$), indicating fair homogeneity of LV shape in MI at end-systole. Correspondingly, the diastole-to-systole change in curvedness (%Δ*C*) was significantly lower, and the variation of %Δ*C* was higher in MI patients compared to normal group, indicating ventricular functional non-uniformity due to the pathologic state.

| | Control (*n*=10) | MI (*n*=11) | p value |
|---|---|---|---|
| Age (years) | 41 ± 16 | 60 ± 6 | 0.003 |
| Weight (kg) | 67 ± 15 | 65 ± 14 | 0.30 |
| Height (cm) | 169 ± 8 | 165 ± 10 | 0.86 |
| Diastolic pressure (mmHg) | 73 ± 12 | 74 ± 18 | 0.79 |
| Systolic pressure (mmHg) | 122 ± 17 | 116 ± 20 | 0.50 |
| HR (beats/min) | 70 ± 9 | 84 ± 13 | 0.012 |
| CI (L/min/m$^2$) | 3.3 ± 0.4 | 2.2 ± 0.5 | <0.001 |
| EDVI (ml/m$^2$) | 73 ± 10 | 148 ± 40 | <0.001 |
| ESVI (ml/m$^2$) | 26 ± 6 | 122 ± 38 | <0.001 |
| EF (%) | 65 ± 5 | 18 ± 5 | <0.001 |
| Sphericity index | 0.52 ± 0.06 | 0.62 ± 0.08 | 0.01 |
| LV mass index | 56 ± 12 | 83 ± 13 | 0.004 |

Table 2. Characteristics of Normal Control and Patients after MI, involved in the study.

| | Controls (*n*=10) | | | MI (*n*=11) | | |
|---|---|---|---|---|---|---|
| Segment | $C_{ED}$(x10$^{-2}$ mm$^{-1}$) | $C_{ES}$(x10$^{-2}$ mm$^{-1}$) | Δ*C* (%) | $C_{ED}$(x10$^{-2}$ mm$^{-1}$) | $C_{ES}$(x10$^{-2}$ mm$^{-1}$) | Δ*C* (%) |
| 1. Basal anterior | 4.1 ± 0.8 | 5.6 ± 0.7 | 38 ± 22 | 3.4 ± 0.5* | 3.7 ± 0.5ξ | 7 ± 17# |
| 2. Basal anterior septal | 3.4 ± 0.6 | 5.3 ± 1.1 | 57 ± 30 | 3.7 ± 1.0 | 3.7 ± 0.9* | 4 ± 26ξ |
| 3. Basal inferior septal | 3.1 ± 0.5 | 4.8 ± 0.6 | 61 ± 25 | 3.6 ± 0.9 | 4.0 ± 1.0* | 12 ± 23ξ |
| 4. Basal inferior | 4.0 ± 0.5 | 5.8 ± 1.0 | 45 ± 27 | 3.7 ± 1.0 | 4.1 ± 1.0* | 13 ± 21* |
| 5. Basal inferior lateral | 3.5 ± 0.5 | 5.3 ± 0.9 | 50 ± 22 | 3.0 ± 0.6* | 3.3 ± 0.9ξ | 13 ± 25* |
| 6. Basal anterior lateral | 3.6 ± 0.8 | 5.0 ± 0.7 | 46 ± 26 | 3.1 ± 0.8 | 3.2 ± 0.8ξ | 8 ± 24* |
| 7. Middle anterior | 3.9 ± 0.5 | 6.0 ± 0.1 | 56 ± 20 | 3.4 ± 0.2* | 3.6 ± 0.3ξ | 6 ± 12ξ |
| 8. Middle anterior septal | 3.9 ± 0.4 | 0.6 ± 1.4 | 55 ± 26 | 3.3 ± 0.6* | 3.4 ± 0.4ξ | 5 ± 17ξ |
| 9. Middle inferior septal | 3.6 ± 0.6 | 5.2 ± 1.1 | 44 ± 18 | 3.5 ± 0.7 | 3.4 ± 0.5ξ | 1 ± 16ξ |
| 10. Middle inferior | 4.1 ± 0.5 | 6.0 ± 1.2 | 51 ± 31 | 3.8 ± 0.7 | 4.0 ± 0.7ξ | 7 ± 17* |
| 11. Middle inferior lateral | 3.6 ± 0.3 | 5.5 ± 0.8 | 52 ± 25 | 3.1 ± 0.6* | 3.4 ± 0.6ξ | 10 ± 14ξ |
| 12. Middle anterior lateral | 3.2 ± 0.3 | 4.7 ± 0.9 | 45 ± 19 | 2.9 ± 0.5 | 3.0 ± 0.3ξ | 4 ± 14ξ |
| 13. Apical anterior | 4.8 ± 1.0 | 9.3 ± 2.0 | 96 ± 33 | 3.8 ± 0.7* | 4.1 ± 1.0ξ | 6 ± 15ξ |
| 14. Apical septal | 4.9 ± 0.6 | 9.0 ± 1.9 | 83 ± 34 | 4.4 ± 0.7 | 4.6 ± 0.9ξ | 4 ± 14ξ |
| 15. Apical inferior | 5.7 ± 0.9 | 11 ± 2.8 | 90 ± 44 | 4.7 ± 1.0* | 4.9 ± 1.0ξ | 5 ± 14ξ |
| 16. Apical lateral | 4.4 ± 0.7 | 8.8 ± 2.2 | 103 ± 65 | 3.8 ± 0.4 | 4.0 ± 0.7ξ | 2 ± 12ξ |
| Mean | 4.0 ± 0.4 | 6.5 ± 1.0 | 61 ± 18 | 3.6 ± 0.5* | 3.8 ± 0.5ξ | 7 ± 9ξ |
| Coefficient of variation (%) | 21 ± 5 | 31 ± 8 | 51 ± 14 | 19 ± 5 | 18 ± 4ξ | 392 ± 501* |

*, $p<0.05$; #, $p<0.01$; ξ, $p<0.001$

Table 3. Left ventricular Regional curvedness, Diastole-to-systole change in curvedness (%Δ*C*), Variation of curvedness and %Δ*C* in MI compared to normal state, as defined by equation (1). This table is related to our work in Ref [2].

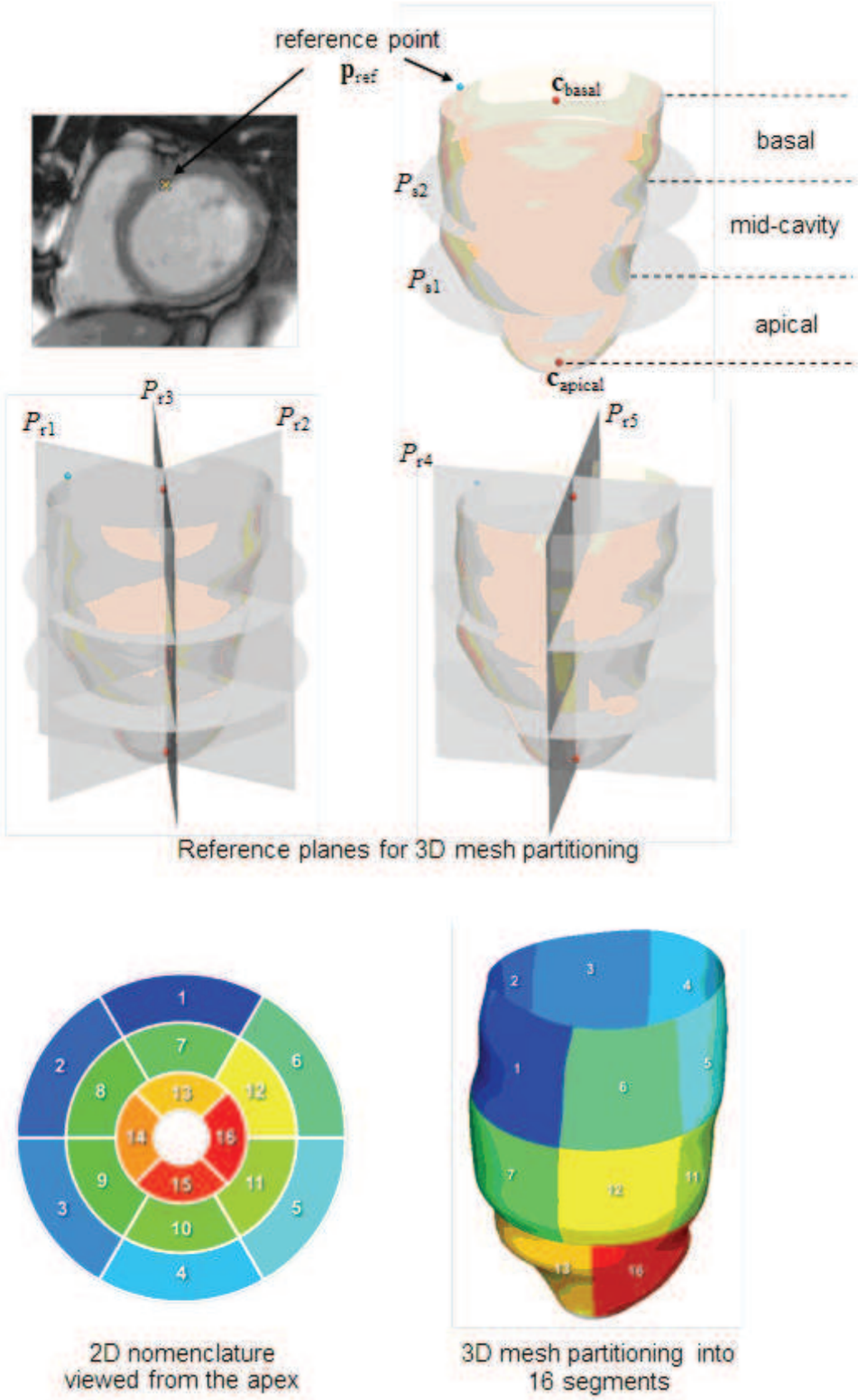


Fig. 3. Partitioning of LV mesh into 16 segments; this figure is based on our work in Ref. [2].

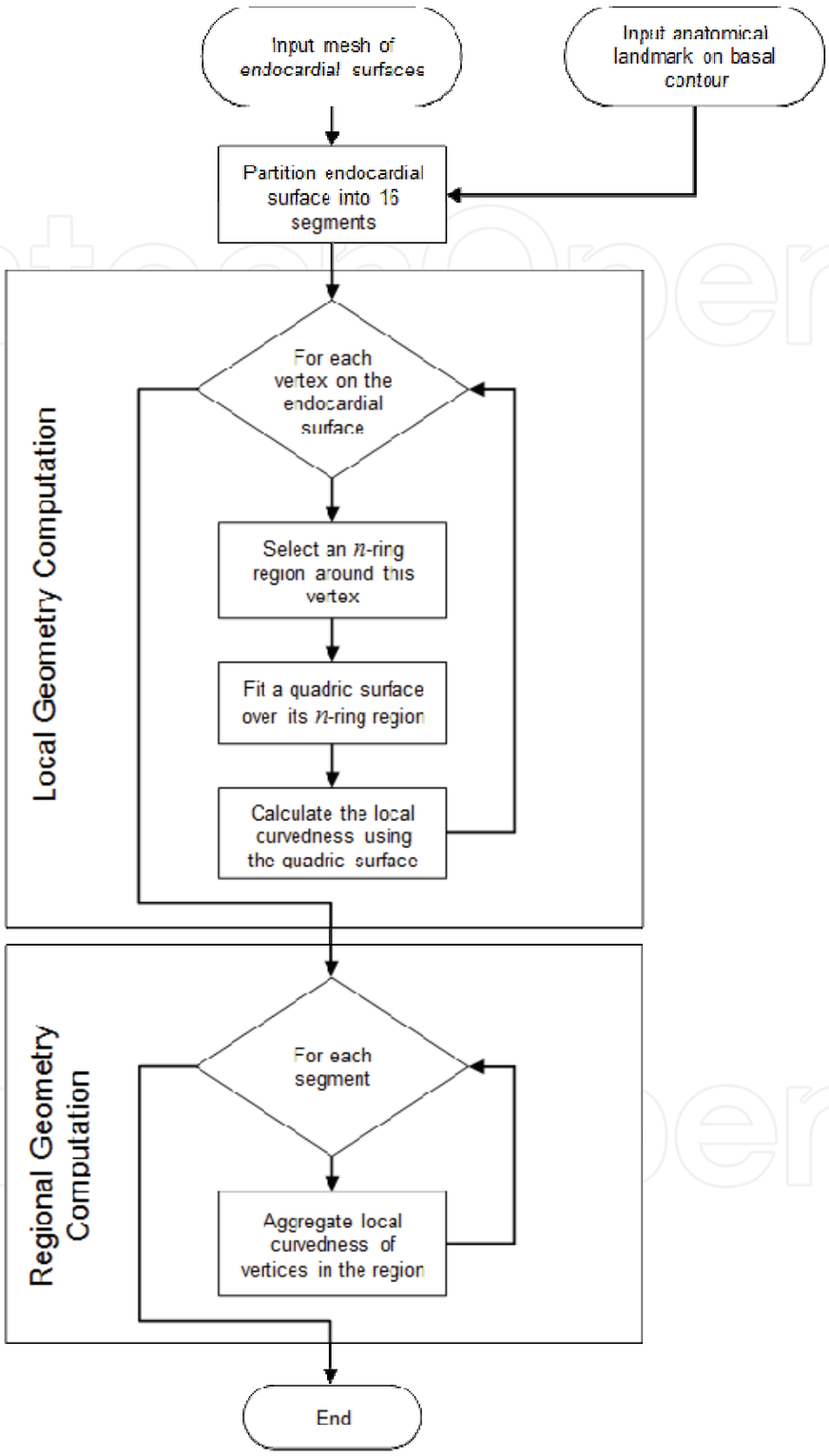


Fig. 4. Flowchart of the overall workflow for the regional LV shape analysis; this figure is based on our work in Ref. [2].

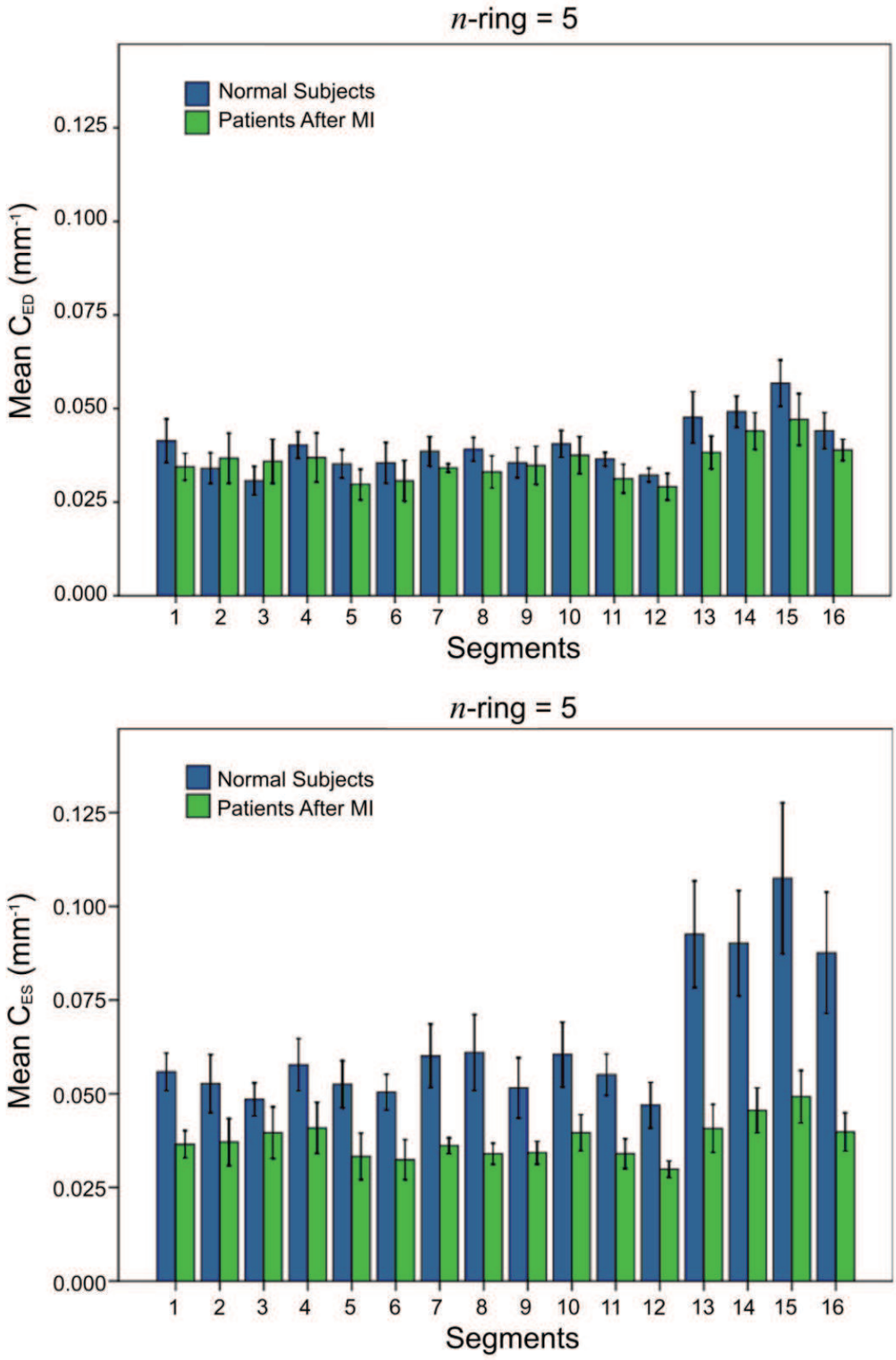


Fig. 5. Comparison of regional curvedness (5-ring selection) in normal subjects and patients after myocardial infarction; this figure is based on our work in Ref. [2].

## 5. Employment of cardiac contractility Index $d\sigma^*/dt_{max}$ to demonstrate (i) its excellent correlation with traditional contractility index $dP/dt_{max}$, in patients with varying ejection fractions, and (ii) its capacity to diagnose Heart failure with normal ejection fraction (HFNEF, or diastolic heart failure) and with reduced ejection fraction (HFREF, or systolic heart failure)

### 5.1 Cardiac contractility expressed in terms of maximum rate of change of pressure-normalized LV wall stress, $d\sigma^*/dt_{max}$

Left Ventricular (LV) contractility can be termed as the capacity of the LV to develop intra-myocardial stress, and thereby intra-cavitary pressure, to eject blood volume as rapidly as possible. It is hence rational and appropriate to formulate a LV contractility index on the basis of LV wall stress. The traditional $dP/dt_{max}$ is based on left ventricular intra-cavitary pressure which is generated by an active myocardial stress. Hence, analogous to $dP/dt_{max}$, which is based on LV intra-cavitary pressure, we have formulated a novel LV contractility index based on LV wall stress, namely the maximum rate of change during systole of LV wall stress normalized to LV intra-cavitary pressure, $d(\sigma/P)/dt_{max}$ or $d\sigma^*/dt_{max}$ , where $\sigma^* = \sigma/P$ [3].

*Model Analysis and Index Formulation:* For mathematically simplicity, we have approximated the LV as a thick-wall spherical shell consisting of incompressible, homogeneous, isotropic, elastic material. The maximum circumferential wall stress ($\sigma_\theta$) can be expressed at the endocardium, as:

$$\sigma_\theta(r_i) = P\left[\frac{r_i^3/r_e^3 + 1/2}{1 - r_i^3/r_e^3}\right] \tag{5}$$

where $r_i$ and $r_e$ are the inner and outer radii, $P$ is LV intracavitary pressure.

By normalizing wall stress to LV intra-cavitary pressure ($P$), we obtain:

$$\sigma^*(r_i) = \frac{\sigma_\theta}{P} = \frac{r_i^3}{r_e^3 - r_i^3}\left(1 + \frac{r_e^3}{2r_i^3}\right) \tag{6}$$

Since the maximum wall stress occurs at the inner endocardial wall, we have:

$$\sigma^*(r = r_i) = \left(\frac{V/(V_m + V) + 1/2}{1 - V/(V_m + V)}\right) = \left(\frac{3V + V_m}{2V_m}\right) = \left(\frac{3V}{2V_m} + \frac{1}{2}\right) \tag{7}$$

where $P$ is LV intra-cavitary pressure; $\sigma_\theta$ is the wall stress; $V$ ($= 4\pi r_i^3/3$) denotes LV volume; $V_m$ ($= 4\pi\left(r_e^3 - r_i^3\right)/3$) denotes LV myocardial volume; $r_i$ and $r_e$ are the inner and outer radii of the LV, respectively. Differentiating equation (7) with respect to time, we get:

$$d\sigma^*/dt_{\max} = \left|\frac{d(\sigma_\theta/P)}{dt}\right|_{max} = \frac{3}{2V_m}\left|\left(\frac{dV}{dt}\right)\right|_{max} \tag{8}$$

It can be thus noted that in contrast to the indices of $dP/dt_{max}$, $E_{es}$ and $E_{a,max}$, our $d\sigma^*/dt_{max}$ index can be determined solely from non-invasive assessment of LV geometry and flow. Normalizing LV wall stress to LV pressure obviates the need for invasive LV pressure measurement.

Our LV contractility formulation has been based on the premise that LV wall stress (due to LV myocardial sarcomere contraction) is responsible for the development of LV pressure. Hence, it is more rational to base LV contractile function on LV wall stress per pressure. Hence, analogus to $dP/dt_{max}$, this LV contractility index is formulated as the maximal rate of pressure-normalized wall stress (as given by the above equation 8), to represent the maximal flow rate out of the ventricle ($dV/dt$) normalized to myocardial volume ($V_m$). This is somewhat in keeping with cardiac output or maximal volume change having been used as a measure of myocardial contractility in rats or human, provided that the influence of afterload is taken into account.

### 5.2 Medical application to subjects with varying ejection fractions, to demonstrate excellent correlation of $d\sigma^*/dt_{max}$ with $dP/dt_{max}$

We have validated $d\sigma^*/dt_{max}$ against $dP/dt_{max}$ and $E_{a,max}$ in 30 subjects with disparate ventricular function in Figure 6, and demonstrated the index's load independence, albeit under conditions of limited preload and after load manipulations [3].

For this study, thirty volunteers [mean 58.1 (range 48–77) yr of age, 13:2 male-to-female ratio] with diverse cardiac conditions were recruited. From their LV pressure-volume data, LVEF and $dP/dt_{max}$ were computed directly from these traces. Active elastance $E$a at various times was also computed from the pressure-volume loops, from the data in Table 4, based on our earlier work on $E$a definition and determination [4]. $E_{a,max}$ was extrapolated from the peak of the $E$a-time curve [4]. The single-beat estimation of end-systolic elastance $E$es (SB) was determined, using bilinearly approximated time-varying elastance [5].

The patients were divided into three groups on the basis of tertiles of LVEF, with 10 individuals in each group, as shown in Table 5. Intergroup comparisons show significant differences between the mean values of $dP/dt_{max}$, $E_{a,max}$, $E$es(SB), and $d\sigma^*/dt_{max}$ in those in the highest tertile compared with those in lowest and middle tertiles. There is agreement with regard to the index $d\sigma^*/dt_{max}$ with $dP/dt_{max}$, $E_{a,max}$, and $E$es(SB) across the three tertiles of ascending LVEF values, with statistically significant differences in LV contractility indexes among the three groups. Values of $dP/dt_{max}$, $E$es(SB), and $d\sigma^*/dt_{max}$ were statistically significantly lower in patients in the lowest and middle tertiles had than those in the highest tertile.

Figure 6 summarizes the correlation between $d\sigma^*/dt_{max}$, $dP/dt_{max}$, and $E_{a,max}$, as well as $E$es(SB). Linear regression analysis revealed good correlation between $d\sigma^*/dt_{max}$ and $dP/dt_{max}$, $E_{a,max}$, and $E$es(SB), with significant correlation coefficients in each case: $d\sigma^*/dt_{max}=0.0075dP/dt_{max}- 4.70$ ($r = 0.88$, $P < 0.01$), $d\sigma^*/dt_{max}=1.20E_{a,max} + 1.40$ ($r = 0.89$, $P<0.01$), and $d\sigma^*/dt_{max}= 1.60E$es(SB) + 1.20 ($r = 0.88$, $P < 0.01$). In contrast, the correlation between $d\sigma^*/dt_{max}$and LVEF is less strong ($r = 0.71$), as is the correlation between $E$es (SB) and LVEF ($r = 0.78$), underscoring the lack of specificity of LVEF as an index of myocardial contractility.

| Frame No. *(i)* | *t*, s | P, mmHg | V, ml | *Ea*, mmHg/ml |
|---|---|---|---|---|
| | | *Isovolumic contraction* | | |
| 1 | 0 | 18 | 136.7 | 0 |
| 2 | 0.02 | 22 | 135.7 | 0.0295 |
| 3 | 0.04 | 32 | 134.6 | 0.1038 |
| 4 | 0.06 | 52 | 133.5 | 0.2536 |
| 5 | 0.08 | 80 | 132.5 | 0.4636 |
| | | *Isovolumic relaxation* | | |
| 18 | 0.34 | 74 | 85.0 | 0.0590 |
| 19 | 0.36 | 50 | 85.5 | 0.1778 |
| 20 | 0.38 | 30 | 86.4 | 0.3127 |
| 21 | 0.40 | 17 | 90.6 | 0.4636 |

Table 4. Active Elastance *Ea computed at discrete time points during isovolumic contraction and relaxation in a sample subject: i*, time instant in the cardiac cycle (frame number from end-diastole); *t*, time from start of isovolumic contraction; *P*, measured left ventricular intracavitary pressure; *V*, measured left ventricular intracavitary volume; $E_{a,i}$, calculated active elastance at instant *i*. This table is related to our work in Ref [4].

| | Lowest tertile | Middle tertile | Highest tertile |
|---|---|---|---|
| Ejection fraction | 0.38 ± 0.12* | 0.49 ± 0.13* | 0.63 ± 0.05 |
| Age,yr | 58.30 ± 8.86 | 56.10 ± 6.15 | 59.90 ± 6.17 |
| Heart rate,beats/min | 71.18 ± 10.72 | 71.77 ± 10.68 | 71.46 ± 9.09 |
| $dP/dt_{max}$,mmHg/s | 960 ± 115* | 1,121 ± 113* | 1,360 ± 97 |
| *E*a,max, mmHg/ml | 0.95 ± 0.32* | 1.85 ± 0.59* | 3.61 ± 0.62 |
| *E*es(SB),mmHg/ml | 0.72 ± 0.26* | 1.51 ± 0.20* | 2.81 ± 0.51 |
| $d\sigma^*/dt_{max}$,$s^{-1}$ | 2.30 ± 0.58* | 3.60 ± 1.06* | 5.64 ± 1.13 |

Table 5. *LV contractility indexes classified into tertiles of LVEF:* Left ventricular contractility indices classified into tertiles of left ventricular ejection fraction. Values are expressed as mean ± standard deviation. Asterisks denote statistically significant difference ($p<0.05$) when compared with corresponding values in the highest tertile of left ventricular ejection fraction. $dP/dt_{max}$, peak first time-derivative of the ventricular pressure; $E_{a,max}$, maximum left ventricular elastance; *E*es(SB), single-beat LV end-systolic elastance; $d\sigma^*/dt_{max}$,left ventricular contractility index. This table is related to our work in Ref [3].

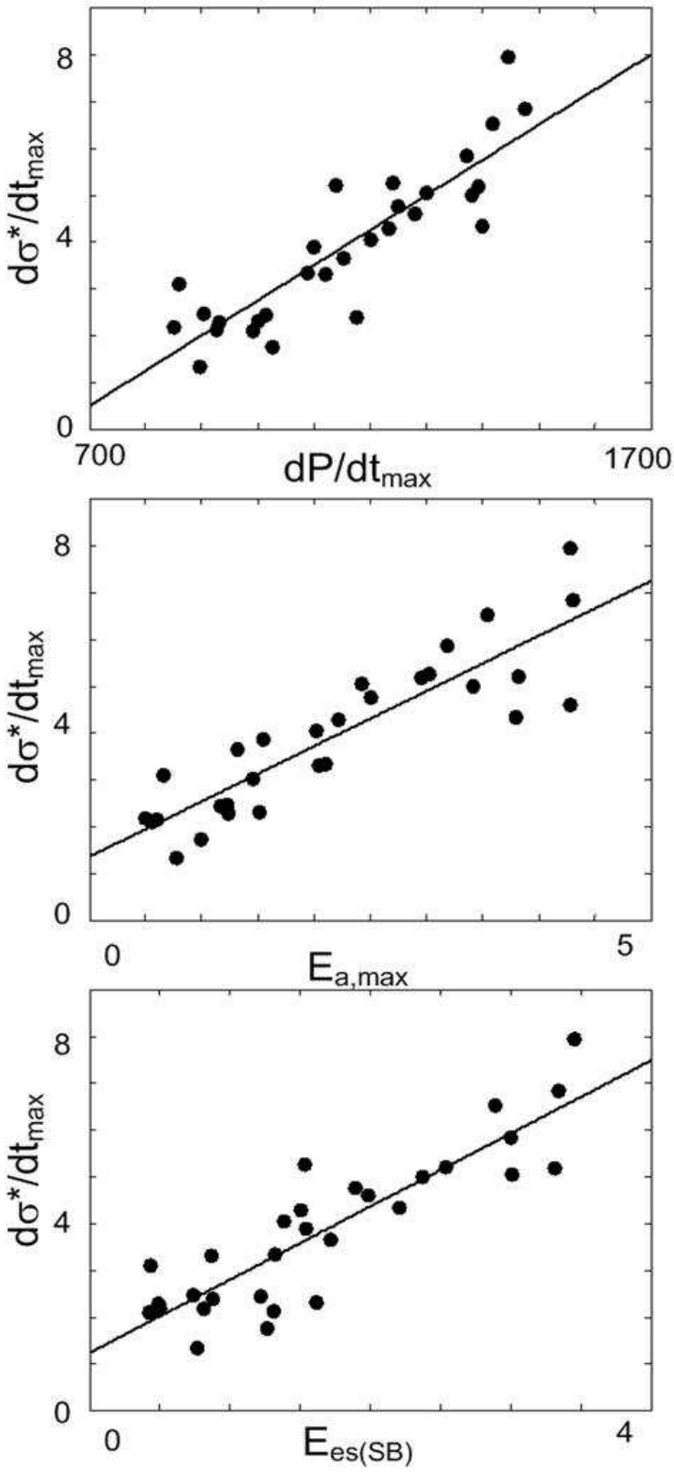


Fig. 6. Linear regression analysis demonstrates good correlation between $d\sigma^*/dt_{max}$ and $dP/dt_{max}$ : [$d\sigma^*/dt_{max} = 0.0075dP/dt_{max}$-4.70, r=0.88; top figure], between $d\sigma^*/dt_{max}$ and $E_{a,max}$ [$d\sigma^*/dt_{max} = 1.20E_{a,max}$+1.40, r=0.89; middle figure], and between $d\sigma^*/dt_{max}$ and $E_{es(SB)}$ [$d\sigma^*/dt_{max} = 1.60E_{es(SB)}$+1.20, r=0.88; bottom figure]. This figure is based on our work in Ref [3].

### 5.3 Use of cardiac contractility index $d\sigma^*/dt_{max}$ to diagnose heart failure with normal ejection fraction (HFNEF) and with reduced ejection fraction (HFREF)

In another study [6], we assessed the capacity of $d\sigma^*/dt_{max}$ to diagnose heart failure in patients with normal ejection fraction (HFNEF) and with reduced ejection fraction (HFREF).

#### 5.3.1 Introduction

Heart failure (HF) is a major health care burden: it is the leading cause of hospitalization in persons older than 65 years, and confers an annual mortality of 10%. HF can occur with either normal or reduced LV ejection fraction (EF), depending on different degrees of ventricular remodeling. Both heart failure with normal ejection fraction (HFNEF) and heart failure with reduced ejection fraction (HFREF), also commonly known as diastolic and systolic heart failure respectively, have equally poor prognosis [7]. Medical therapy targets to reduce load, by using vasodilators and/or to alter contractile strength using inotropic agents. Alternatively, some therapies target to affect cardiac remodeling, such as passive cardiac support devices, surgical restoration of LV shape (i.e. the Dor procedure), and stem cells therapies.

Assessment of left ventricular (LV) contractility is important for HF management and evaluation of the heart's response to medical and surgical therapies. Although approaches based on pressure-volume analysis, stress-strain analysis, and $dP/dt_{max}$-EDV relations [8]can provide assessments of contractile function, these relations generally require invasive data measured at several chamber loads and thus are difficult to apply in routine or long-term clinical studies. This is an important limitation, because heart failure often requires longitudinal evaluation. The ideal measure of contractility should have the following characteristics: sensitivity to inotropic changes, independence from loading conditions as well as heart size and mass, ease of application, and proven usefulness in the clinical setting. LV ejection fraction (EF) is the index overwhelmingly used to assess cardiac function in both clinical and experimental studies, despite the fact that it is highly dependent upon preload and afterload. Based on the National Heart Lung and Blood Institute's Framingham Heart Study, an LVEF50% as cut-off for the presence of normal LVEF has been used in the present study [9].

**Usefulness of $d\sigma^*/dt_{max}$ as Contractility Index:** During LV systole, LV wall stress is generated intrinsically by sarcomere contraction and results in the development of extrinsic LV pressure. We have shown earlier that our novel LV contractility index, $d\sigma^*/dt_{max}$ (maximal change rate of pressure-normalized wall stress) correlates well with LV $dP/dt_{max}$ [3]. We have proposed and validated a new LV contractility index, $d\sigma^*/dt_{max}$ ,based on the maximal rate of development of LV wall stress with respect to LV pressure. From the right-hand side of equation (8), this index is also seen to represent the maximal flow rate from the ventricle (cardiac output) normalized to myocardial volume (or mass).

This index is easily measured non-invasively (i.e. from echocardiography or magnetic resonance imaging), is sensitive to LV inotropic changes, and has been demonstrated by us to be preload and afterload independent [3]. Importantly, it is measured at a single steady-state condition, as opposed to the multiple variably loaded cardiac cycles required for many of the other indices. Thus $d\sigma^*/dt_{max}$has several qualities that make it a useful LV contractility index. This study [6] has constituted an important step toward establishing the clinical utility of $d\sigma^*/dt_{max}$ as a tool for diagnosis of HF (both HFNEF and HFREF) as well as for

follow-up surveillance of LV function. Hence we see a great potential for application of this novel index to evaluate heart function in diverse heart conditions.

### 5.3.2 Clinical methodology

Patients referred to our echocardiography service with symptoms and signs of heart failure underwent echocardiography and electrocardiography (ECG). Patients with atrial fibrillation, more than mild mitral or aortic valvular regurgitation, and unsatisfactory echocardiographic images were excluded. Clinical signs of heart failure were defined as presence of at least one of the following: raised jugular venous pressure, peripheral pedema, hepatomegaly, basal inspiratory crepitation or gallop rhythm. Patients with LVEF ≥ 50% and LVEF < 50% on echocardiography were classified into HFNEF and HFREF, respectively.

*Echocardiography Study:* With the subject in the left lateral decubitus position, 2D examinations, M-mode measurements and Doppler recordings were performed from the standard left parasternal long- and short-axis as well as the apical four chamber views with simultaneous ECG. The LVEF was assessed by using a 2-dimensional method by an experienced observer; normal LVEF was defined as greater or equal to 50%. Mitral flow velocities were obtained from the apical 4-chamber view using pulsed wave Doppler technique with the sample volume at the tips of the corresponding valve leaflets. LV outflow tract velocity was obtained from apical 5-chamber view, using pulsed wave Doppler technique with the sample volume at the aortic valve level.

The measurements included peak E (peak early trans-mitral filling velocity during early diastole) and A (peak trans-mitral atrial filling velocity during late diastole); wave velocities (cm/s) were measured and E/A ratio was calculated. The E wave deceleration time (DT) was also calculated as the time elapsed between peak E velocity and the point where the extrapolation of the deceleration slope of E velocity crosses the zero baseline measured in milliseconds. LVOT maximal velocity $V_{peak}$ was measured, and LV mass was calculated by using ASE methods [10, 11]. Myocardial tissue Doppler (TDI) velocities were also estimated at the atrioventricular ring, septal positions, in the apical 4 chamber view. All measurements were averaged over two or three cardiac cycle.

**Calculation of** $d\sigma^*/dt_{max}$ *from Echocardiography:* The contractility index was computed by the above equation (8). M-mode echocardiographic measurements of the LV were obtained, and LV mass calculated using standardized methodology [10, 11]. Myocardial volume was calculated by dividing LV mass with myocardial density (assumed to be 1.05 g/ml). Furthermore, two-dimensional apical four- and two-chamber views of the LV were acquired, and end-diastolic and –systolic endocardial contours were manually outlined. The corresponding LVEDV were then automatically determined using biplane Simpson's method.

From Pulse-wave echo-Doppler interrogation of the LV outflow tract (LVOT), we calculated (in the absence of significant mitral regurgitation or aortic valve dysfunction) the maximal LV volume rate ($dV/dt_{max}$) during ejection: $dV/dt_{max}=V_{peak}$*AVA, where $V_{peak}$ is the peak velocity sampled at the LVOT and AVA is the aortic valve area (= $\pi D^2/4$, where $D$ is the LVOT diameter measured in the two-dimensional parasternal long-axis image of the heart), as shown in Figure 7. Upon substituting values of myocardial volume and $dV/dt_{max}$ into equation (8), we determined the value of $d\sigma^*/dt_{max}$ .

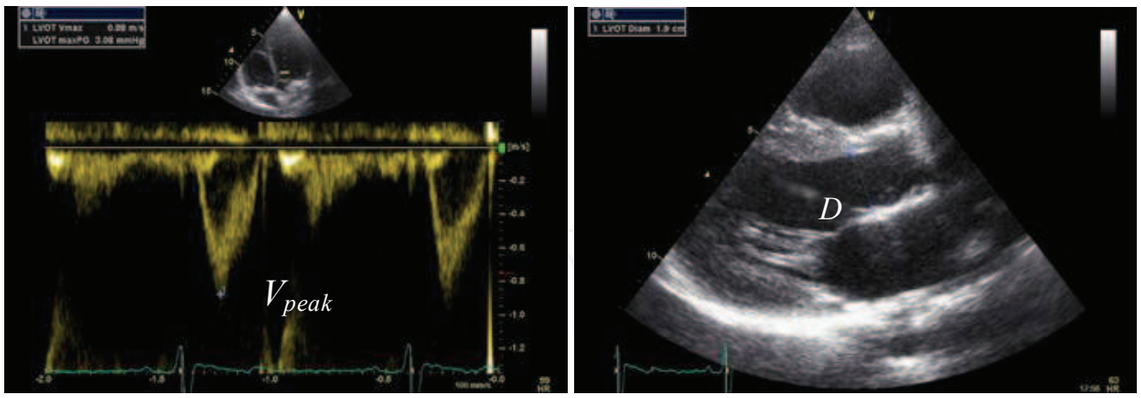


(a) (b)

Fig. 7. Echocardiographic measurement on (a) peak velocity $V_{peak}$ sampled at the LVOT and (b) LVOT diameter $D$ measured in the two-dimensional parasternal long-axis image of the heart. This figure is adopted from Ref. [6].

**Clinical Studies:** The study involved 26 age- and sex-matched subjects in each of the groups of normal controls, HFNEF and HFREF. The characteristics of 78 subjects are shown in Table 6. It summarizes the subjects' age, BSA, LVEF, peak E, peak A, E/A ratio, DT, heart rate (HR), septal E/E', lateral E/E' and our index $d\sigma^*/dt_{max}$. Mean $d\sigma^*/dt_{max}$ was 3.91 $s^{-1}$ (95%CI, 3.56-4.26 $s^{-1}$) in control subjects; it was reduced in heart failure, HFNEF, to 2.90 $s^{-1}$ (95%CI, 2.56-3.24 $s^{-1}$); and in HFREF, to 1.84 $s^{-1}$ (95%CI, 1.60-2.07 $s^{-1}$). There exists no substantially difference between the average values of LVEF, peak E, peak A, E/A ratio, DT, heart rate (HR), septal E/E', and lateral E/E' in HENEF compared to normal controls, except for $d\sigma^*/dt_{max}$ (2.90 ± 0.84 vs. 3.91 ± 0.87, $p$<0.001). However, there exists significant difference between the average values of LVEF, peak E, peak A, E/A ratio, DT, septal E/E', lateral E/E' and $d\sigma^*/dt_{max}$ in HEREF compared to HFNEF.

**Discussion on the Usefulness of $d\sigma^*/dt_{max}$:** During LV systole, LV wall stress is generated intrinsically by sarcomere contraction and results in the development of extrinsic LV pressure. LV wall stress is dependent on wall thickness, LV geometry and chamber pressure and sarcomere contraction. Hence, it is rational to quantify the LV wall stress as an intrinsic measure of myocardial contractility. We have proposed and validated a new LV contractility index, $d\sigma^*/dt_{max}$,based on the maximal rate of development of LV wall stress with respect to LV pressure. From the right-hand side of equation (8),this index is also seen to represent the maximal flow rate from the ventricle (cardiac output) normalized to myocardial volume (or mass).

**Assessment of heart failure with normal ejection fraction (HFNEF) and reduced ejection fraction (HFREF):** Heart failure may be viewed as a progressive disorder that is initiated after an "index event" with a resultant loss of functioning cardiac myocytes, thereby preventing the heart from contracting normally. HF can occur with either normal or reduced LV ejection fraction (LVEF), depending on different degree of ventricular remodeling. Perhaps 50% of patients with heart failure have a normal or minimally impaired LVEF (HFNEF) [12, 13].

Although mechanisms for HFNEF remain incompletely understood, diastolic dysfunction is said to play a dominant role: impaired relaxation, increased passive stiffness, raised end-

diastolic pressure (EDP) [14]. The diagnostic standard for HFNEF is cardiac catheterization, which demonstrates increased EDP. However, a more practical noninvasive alternative is echocardiography. Our study has shown that E/A ratio (1.26 ± 0.90 vs. 0.96 ± 0.38, p<0.05) and DT (157 ± 41 ms vs. 214 ± 47 ms, p<0.05) are significantly different between HFREF and normal controls, and not so between HFNEF and normal controls (Table 6).

Our contractility index, of change rate of normalized wall stress index $d\sigma^*/dt_{max}$, is dependent on lumen and wall volume of LV chamber and represents an integrated assessment of LV systolic performance [3], based on our findings relating $d\sigma^*/dt_{max}$ with HFNEF and HFREF [6]. In this study, as shown in Table 7, we find that there exists significant difference in $dV/dt_{max}$ between HFREF and HFNEF (233±48 ml/s vs. 355±65 ml/s, $p$<0.05), while there exists no difference between HFNEF and normal controls (355±65 ml/s vs. 353±80 ml/s, *NS*). Similarly, there exists significant difference in LV mass between normal controls and HFNEF (147±41 g vs. 202±47 g, $p$<0.05), while there is no difference between HFREF and HFNEF (213±60 g vs. 202±47 g, *NS*).

Our $d\sigma^*/dt_{max}$ index, using $dV/dt_{max}$ normalized with LV mass, can clearly differentiate HFREF, HFNEF and normal controls (p<0.05) (Table 7). The average value of $d\sigma^*/dt_{max}$ decreases in HFNEF and HFREF, in relation to normal controls. The mean value of $d\sigma^*/dt_{max}$ was found to be 3.91 $s^{-1}$ (95%CI, 3.56-4.26 $s^{-1}$) in control subjects; the index was reduced in heart failure patients: in HFNEF, to 2.90 $s^{-1}$ (95%CI, 2.56-3.24 $s^{-1}$) and in HFREF, to 1.84 $s^{-1}$ (95%CI, 1.60-2.07 $s^{-1}$). This suggests that poor systolic function of LV is associated with lower $d\sigma^*/dt_{max}$ values. Therefore, it can again be concluded that $d\sigma^*/dt_{max}$ is an appropriate index for representing assessment of LV contractile function in heart failure with/without preserved LV ejection fraction.

| | Controls (n=26) (n=21) | HFNEF (n=26) | HFREF (n=26) |
|---|---|---|---|
| Age (years) | 72 ± 8 | 70 ± 8 | 70 ± 8 |
| Gender (male:female) | 16:10 | 16:10 | 16:10 |
| BSA ($m^2$) | 1.69 ± 0.20 | 1.71 ± 0.20 | 1.61 ± 0.20 |
| LVEF (%) | 68.3 ± 5.1 | 66.5 ± 4.9 | 33 ± 13.7§* |
| E/A ratio | 0.96 ± 0.38 | 0.78 ± 0.24 | 1.26 ± 0.90* |
| DT (ms) | 214 ± 47 | 214 ± 67 | 157 ± 41§* |
| HR (beats/min) | 66 ± 10 | 72 ± 16 | 80 ± 11§ |
| Septal E/E' | 8.48 ± 2.10 | 9.79 ± 3.29 | 13.68 ± 4.78§* |
| Lateral E/E' | 6.64 ± 1.55 | 8.39 ± 2.76 | 10.28 ± 3.40§* |
| $d\sigma^*/dt_{max}$ ($s^{-1}$) | 3.91 ± 0.87 | 2.90 ± 0.84§* | 1.84 ± 0.59§* |

A, mitral atrial flow velocity on echo-Doppler; BSA, body surface area; DT, mitral E deceleration time; E, mitral early velocity; E', septal mitral annular myocardial velocity on tissue Doppler imaging; HR, heart rate, LVEF, let ventricular ejection fraction.

The values are expressed as mean ± SD. § and * denote statistically significant difference of HF compared to controls, HFREF compared to HFNEF patients, respectively (Bonferroni pairwise test, $p$ value <0.05)

Table 6. Patients characteristics and echocardiographic measurements in Group 1 (Controls), Group 2 (HFNEF) and Group 3 (HFREF). This table is related to our work in Ref [6].

| | Controls (95% CI) | HFNEF (95% CI) | HFREF (95% CI) |
|---|---|---|---|
| $dV/dt_{max}$ (ml/s) | 353 (320, 385) | 355 (329, 381) | 233 (213, 252)§* |
| $V_{peak}$(cm/s) | 106 (98, 115) | 112 (104, 119) | 73 (68, 78) §* |
| LV mass (g) | 147 (131, 164) | 202 (183, 221)§ | 213 (189, 297)§ |
| $d\sigma^*/dt_{max}$ ($s^{-1}$) | 3.91 (3.56, 4.26) | 2.90 (2.56, 3.24)§* | 1.84 (1.60, 2.07)§* |

§ and * denote statistically significant difference of HF compared to controls, HFREF compared to HFNEF patients, respectively

Table 7. Comparison of the maximal flow rate $dV/dt_{max}$, $V_{peak}$, LV mass, and $d\sigma^*/dt_{max}$ in Group 1 (Controls), Group 2 (HFNEF) and Group 3 (HFREF). This table is related to our work in Ref [6].

## 6. Coronary Arterial Bypass Grafting (CABG) to salvage ischemic myocardial segments

As is well known, coronary artery bypass graft (CABG) surgery has been the standard treatment for serious blockages in the coronary arteries and for re-perfusing myocardial ischemic segments to restore them to normal contractile state. During the surgery, one end of the graft is sewn to the aorta (or its subsidiary branches) to create proximal anastomosis, while the other end is attached to coronary artery below the area of blockage to create distal anastomosis. In this way, the oxygen-rich blood is taken directly from the aorta, bypasses the obstruction, and flows through the graft to perfuse and nourish the heart muscle. The most commonly used graft is the saphenous vein. Besides this vein graft, some arterial conduits (such as internal mammary artery, gastroepiploic artery and radial artery etc), and synthetic veins (such as Dacron, Teflon and Polytetrafluoroethylene-PTFE veins) are also suitable for CABG.

Although the number of bypass operations keeps increasing, the CABG has not been without complications. Approximately 15% to 20% vein grafts occlude in the first year, and 22.5% to 30% occlude within the first 2 years. At 10 years, approximately 60% of vein grafts are patent; only 50% of these vein grafts remain free of significant stenosis. In order to intensively investigate the coronary arterial stenosis symptom, numerous research works have been carried out. One direction of these studies is to investigate the pathogenic mechanism of bypass graft failure. In this regard, vascular injury and biomechanical factors (such as wall shear stress related factors, compliance mismatch, etc.) are believed to stimulate cellular responses for pathological changes. In particular, hemodynamic flow patterns of CABG have considerable relevance to the causes and sites of pathogenesis. Hence, we have carried out simulation of hemodynamic flow patterns in CABG models, to look into the hemodynamic causes and mechanisms of lesions in coronary bypass grafts.

The flow characteristics and hemodynamic parameters distributions in a complete CABG model (as shown in Figure 8) have been investigated computationally by us [15]. It is found that disturbed flow (flow separation and reattachment, vortical and secondary flows) patterns occur at both proximal and distal anastomoses, especially at the distal anastomosis. In addition, regions of high-OSI & low-WSS and low-OSI & high-WSS are found in the proximal and distal anastomoses, especially at the toe and heel regions of distal anastomosis. These regions are suspected to initiate the atherosclerotic lesions and are further worsened by the increasing permeability of low-density lipoprotein as indicated by high WSSG. The comparisons of segmental average of HPs (in the Table of Figure 8) further

imply that intimal hyperplasia is more prone to form in the distal anastomosis than the proximal anastomosis, especially along the suture line at the toe and heel of distal anastomosis, which was in line with the in-vivo observations.

We then investigated the fluid dynamics of blood flow in two complete models of CABG for the right and left coronary artery separately, as shown in Figure 9 [16]. The results reveal that blood flow through the coronary artery bypass graft primarily occurs only during the diastolic phase of the cardiac cycle, which is in agreement with the physiological observation. However, at the onset of ejection, some backflow from the coronary artery into the bypass graft is found for the CABG to left coronary artery, which is absent for the right coronary artery. This reversal of flow during systole can be explained by the predominant intra-cardiac course of the left coronary artery system. As the same time, this study also found a low WSS region near the heel and a high WSS in the toe region of the anastomosis domain.

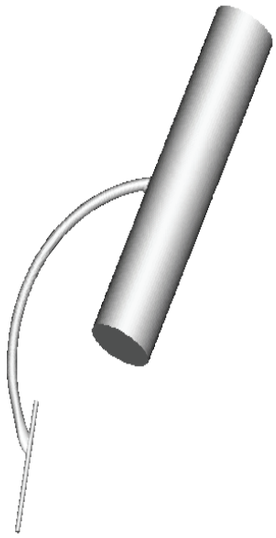

(a)

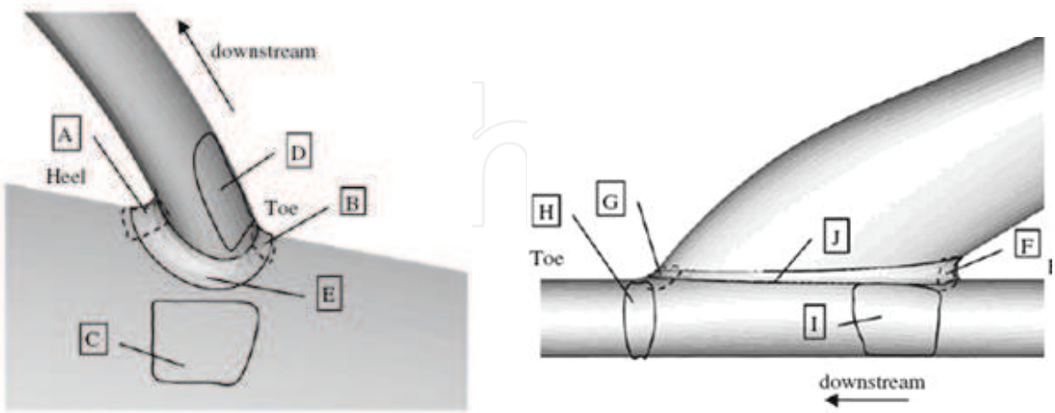


(b)

Fig. 8. (a) The configuration to mimic complete CABG; (b) sketch maps of areas investigated for segmental averages of hemodynamic parameters (HPs) in proximal and distal anastomoses;

| Name | | Labels in maps | Area (mm²) | <WSS> (Pa) | <WSSG> | <OSI> |
|---|---|---|---|---|---|---|
| Proximal anastomosis | heel | A | 4.23 | 4.48 | 11.88 | 0.41 |
| | toe | B | 1.59 | 8.58 | 20.24 | 0.36 |
| | part3 | C | 9.46 | 3.17 | 3.24 | 0.49 |
| | part4 | D | 25.50 | 6.56 | 14.25 | 0.07 |
| | suture_line | E | 12.00 | 5.06 | 9.01 | 0.29 |
| Distal anastomosis | heel | F | 0.55 | 2.92 | 12.75 | 0.24 |
| | toe | G | 0.55 | **28.04** | **147.17** | **0.02** |
| | part3 | H | 9.70 | **14.63** | **64.24** | **0.07** |
| | part4 | I | 6.81 | 0.85 | 3.59 | 0.22 |
| | suture_line | J | 3.18 | **9.20** | **41.43** | **0.11** |

(c)

Fig. 8. (c) the segmental averages of HPs at these locations. This figure is adopted from our work in Ref 15 (Zhang et al., 2008).

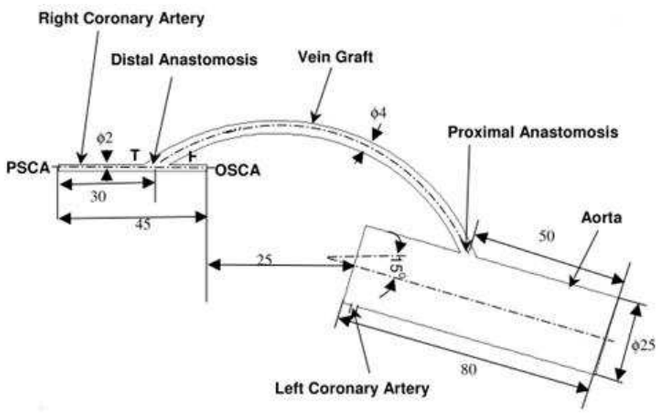


(a)

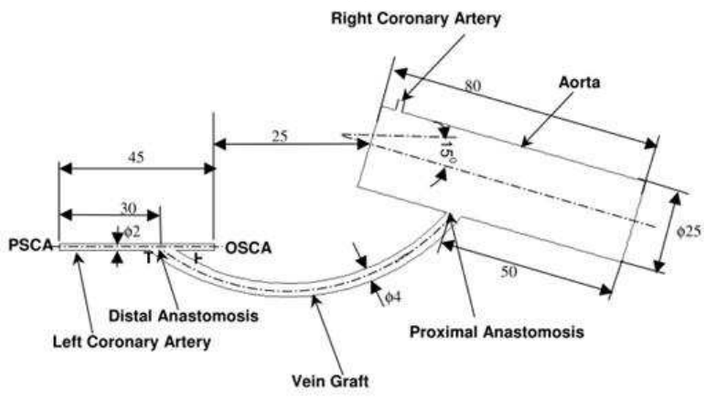


(b)

Fig. 9. Geometry (plane view) and dimensions (in mm) of the bypass models of: (a) The aorta-right coronary artery bypass model; (b) The aorta-left coronary artery bypass model (PSCA-Perfused Segment of the Coronary Artery; OSCA-Occluded Segment of the Coronary Artery; T-Toe; H-Heel). This figure is adopted from our work in Ref 16: (Sankaranarayanan et al., 2005).

CABG performance is based on flow characteristics at both the proximal and distal anastomoses. So then, let us summarise the optimal geometrical parameters for proximal and distal anastomoses. For proximal anastomosis, a detailed study, on the effect of three grafting angles (viz. 45° forward facing, 45° backward facing, and 90°), has been carried out by Chua et al. [17]. The results show a flow separation region along the graft inner wall immediately after the heel at peak flow phase, which decreases in size with the grafting angle shifting from 45° forward facing to 45° backward facing. The existence of nearly fixed stagnating location, flow separation, vortex, high-WSS-low-OSI, low-WSS-high-OSI, and high WSSG is suspected to lead to graft stenosis. Among these three models, the 45° backward-facing graft is found to have the lowest variation range of time-averaged WSS and the lowest segmental average of WSSG, as shown in Figure 10; these parameters are then recommended for obtaining higher expected patency rates in bypass operations.

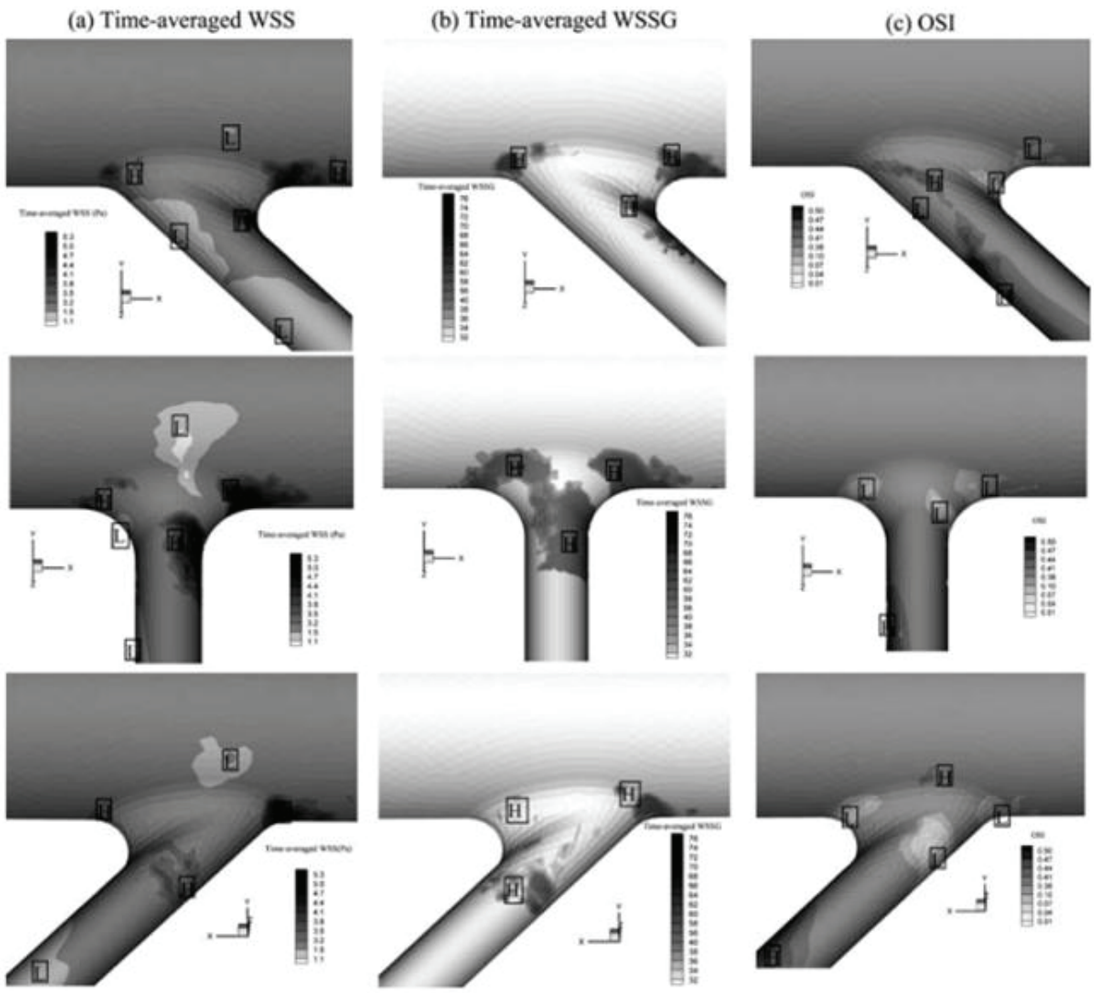


Fig. 10. Contours of HPs: (a) time-averaged WSS; (b) time-averaged WSSG; and (c) OSI, on the surfaces of 45° forward-facing, 90°, and 45° backward-facing models ('H' means the region has high value, 'L' means the region has low values. This figure is adopted from our work in Ref 17 (Chua et al., 2005b).

At the distal anastomosis junction of CABG, the important geometrical parameters for smooth flow are the angle (α) and the diameter ratio (ϕ) between the graft and host artery. The hemodynamics associated with these parametric were investigated by Xiong and Chong [18], over a range of ϕ (1:1, 1.5:1 and 2:1) and α (15°, 30°, 45° and 60°) in physiological coronary flow conditions. It is found that increasing ϕ from 1:1 to 1.5:1 almost eliminates both low WSS and high OSI at the toe. However, further increasing ϕ to 2:1 causes elevated OSI for most of the host artery segment in the anastomotic region and in almost the entire graft. On the other hand, varying α is also found to change certain aspects of hemodynamics, although less than those changes related with different values of ϕ. A smaller value of α is found to be associated with a higher OSI in the anastomotic region, whereas a larger α causes higher WSSG on the artery floor. Therefore, it is suggested that for distal coronary anastomosis (with a 20:80 proximal to distal flow division ratio maintained in the host artery), the geometry associated with ϕ = 1.5 and α = 30–45° is favorable for enhancing long-term performance.

## 7. Surgical Ventricular Restoration (SVR), combined with CABG, restores LV shape and improves cardiac contractility

### 7.1 Introduction

Ischemic heart disease is one of the most widely spread, progressive and prognostically unfavorable diseases of the cardiovascular system. In ischemic dilated cardiomyopathy (IDC) patients, the remodeling process involves a lesser systolic LV curved shape, increase of peak wall stress, and decrease of contractile functional index, compared with normal subjects. Surgical ventricular restoration (SVR) is performed in chronic ischemic heart disease patients with large non-aneurysmal or aneurysmal post-myocardial infarction zones. It involves operative methods, that reduce LV volume and 'restore' ventricular ellipsoidal shape, by exclusion of anteroseptal, apical, and anterolateral LV scarred segments by means of intra-cardiac patch or direct closure.

For patients in heart failure (HF) resulting from serious myocardial diseases of ischemic dilated cardiomyopathy and myocardial infarction (MI), surgical ventricular restoration (SVR), designed to restore the LV to its normal shape (reversal of LV remodeling), is performed usually in conjunction with coronary artery bypass grafting (CABG). In our study [19], in 40 ischemic dilated cardiomyopathy (IDC) patients who underwent SVR and CABG, there was found to be: (i) decrease in end-diastolic volume from 318 ± 63 ml to 206 ± 59 ml ($p<0.01$) and in end-systolic volume from 228 ± 58 ml to 133 ± 61 ml ($p<0.01$), (ii) increase in LV ejection fraction from 26 ± 7% to 31 ± 8% ($p<0.01$), (iii) decrease in LV mass (from 204 ± 49 g to 187 ± 53 g, $p<0.01$), (iv) decrease in peak normalized wall stress (PNWS) (from 4.30 ± 0.95 to 3.31 ± 0.75, $p<0.01$) , (v) increase in end-systolic sphericity index SI (from 0.57 ± 0.094 to 0.67 ± 0.13, $p<0.01$), (vi) increased value of shape (S) index (from 0.44 ± 0.085 to 0.54 ± 0.089, $p<0.01$) during end-systole indicating that LV became more spherical after SVR, and most importantly (vii) improvement in LV contractility index $d\sigma^*/dt_{max}$ (from 2.69 ± 0.74 $s^{-1}$ to 3.23 ± 0.73 $s^{-1}$, $p<0.01$).

Thus, in IDC patients, surgical ventricular restoration (in combination with CABG) aiming to reverse LV remodeling, has shown to (i) improve ventricular function and decrease wall stress, along with making a more curved apex, and (ii) improve cardiac contractility. It is not the LV shape alone that defines LV contractility. Rather, a complex interaction of the rate of change of shape factor ($dS/dt_{max}$) along with LV maximal flow rate and LV mass may explain the improvement in LV contractility.

### 7.2 Clinical study

The study was carried to retrospectively evaluate (with cardiac MRI) the changes on systolic function and LV wall stress, the relationships between LV geometry (shape) and dimensions and systolic function after SVR performed in chronic ischemic heart disease patients with aneurismal postmyocardial infarction zones. The study consisted of 40 patients with ischemic dilated cardiomyopathy who had SVR; the age of the patients averaged 69 years (range, 52-84 years). MRI scans were performed 2 weeks before surgery (pre-surgery) and 1 week after the surgery; the details of the MRI procedure are reported in our earlier work [19].

Cardiac magnetic resonance imaging (MRI) provides the means to study heart structure and function: the ventricular systolic and diastolic volumes (and hence ejection fraction) are easily assessed reproducibly and accurately; the regional wall motion of the asynergy area and the remote myocardium can be measured by several quantitative means, including with myocardial tagging; the presence or absence of nonviable, irreversible scar can be detected with gadolinium-based interstitial contrast agents.

**Data Analysis, 3-dimensional modeling of LV:** For analysis, the images were displayed on a computer monitor in a cine-loop mode using CMRtools, to reconstruct the 3-dimensional model of the left ventricle (LV). The LV epicardial and endocardial borders were outlined, and all the frames were delineated to produce a volume curve from end-diastolic and end-systolic phases. These measurements were used to determine the end-diastolic volume (EDV), end-systolic volume (ESV), stroke volume (SV), ejection fraction (EF), and LV mass.

*Ellipsoidal Shape factor, Eccentricity (E) and sphericity index and normalized wall stress*: The LV is modeled as a prolate spheroid, truncated 50% of the distance from equator to base, as shown in figure 11 [20, 21]. Then, the left ventricular cavity wall volume is calculated, from the endocardial anterior-posterior (AP) and base-apex (BA) lengths [20], as:

$$V_m = \frac{9}{8}\left[\left(\frac{BA}{1.5}+h\right)\left(\frac{AP}{2}+h\right)^2 - \left(\frac{BA}{1.5}\right)\left(\frac{AP}{2}\right)^2\right] \tag{9}$$

wherein the BA and AP dimensions are identified in figure 12. The mean wall thickness (h) is calculated at each cavity volume, from the above equation, by assuming that myocardial wall volume ($V_m$) remains constant throughout the cardiac cycle. The endocardial minor axis dimension (SA) and major axis dimension (LA), shape factor (S), eccentricity (E) and sphericity index (SI) were then calculated as follows (refer figures 11 and 12):

$$\mathrm{SA} = \mathrm{AP}/2;\ \mathrm{LA} = \mathrm{BA}/1.5,\ \mathrm{S} = \mathrm{SA}/\mathrm{LA},\ \ E = \left(\frac{BA^2 - AP^2}{BA^2}\right)^{0.5},\ \ \mathrm{SI} = \mathrm{AP}/\mathrm{BP} \tag{10}$$

wherein BA (the LV long axis) is defined as the longest distance from the apex to the base of the LV (defined as the mitral annular plane), as measured on the four-chamber cine MRI view of the heart; AP is defined as the widest LV minor axis **(**Figure 12). A small value of SI implies an ellipsoid LV, whereas values approaching "1" suggest a more spherical LV. The SI at end-diastole ($SI_{ed}$) and end-systole ($SI_{es}$), the % shortening of the long and minor axes, as well as the difference between end-diastolic and end-systolic values of SI, ($SI_{ed}$ - $SI_{es}$) were calculated and are tabulated in Table 10 below.

The time-varying circumferential normalized wall stress, NWS(t), is calculated from the instantaneous measurements of LV dimensions and wall thickness, by treating the LV as a prolate spheroid model truncated 50% of the distance from equator to base [20, 21]

$$NWS(t) = \frac{AP(t)}{2h(t)}\left[1 - \frac{\frac{9AP(t)}{32h(t)}(SI)^2}{\frac{AP(t)}{h(t)} + 1}\right] \tag{11}$$

The LV wall thickness, h(t), is calculated from the following formula (based on the above equation 9), by assuming that the myocardial wall volume ($V_m$) remains constant throughout the cardiac cycle:

$$\frac{9}{8}\left[\left(\frac{BA(t)}{1.5} + h(t)\right)\left(\frac{AP(t)}{2} + h(t)\right)^2\right] = V_m(t) + \left(\frac{BA(t)}{1.5}\right)\left(\frac{AP(t)}{2}\right)^2 \tag{12}$$

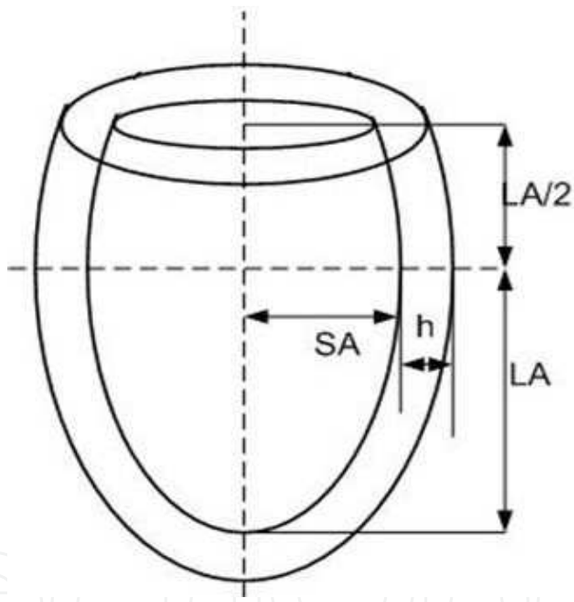


Fig. 11. LV model geometry, showing the major and minor radii of the inner surface of the LV (LA & SA) and the wall-thickness (h).

**Cardicac Contractility** $d\sigma^*/dt_{max}$**:** In order to compute the contractility index by employing the above equation (8), a 6-order polynomial function to curve-fit the volumes-time data to calculate the volume rate ($dV/dt$) by differentiating it. Then the contractility index $d\sigma^*/dt_{max}$ is calculated as:

$$d\sigma^*/dt_{\max} = \left|\frac{d(\sigma_\theta / P)}{dt}\right|_{max} = \frac{3}{2V_m}\left|\left(\frac{dV}{dt}\right)\right|_{max}$$

where $V_m$ is myocardial volume at the end-diastolic phase.

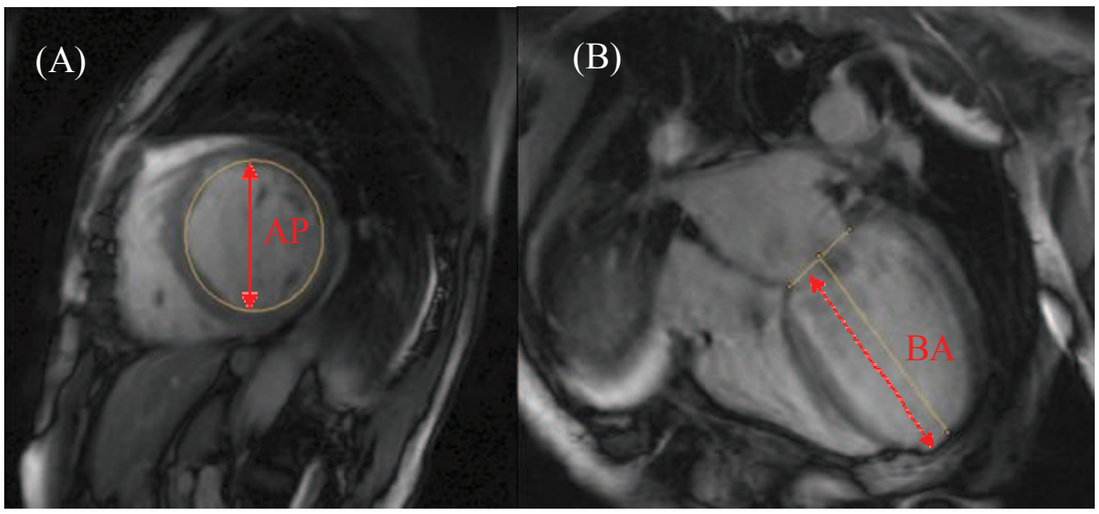


(a) Pre-SVR

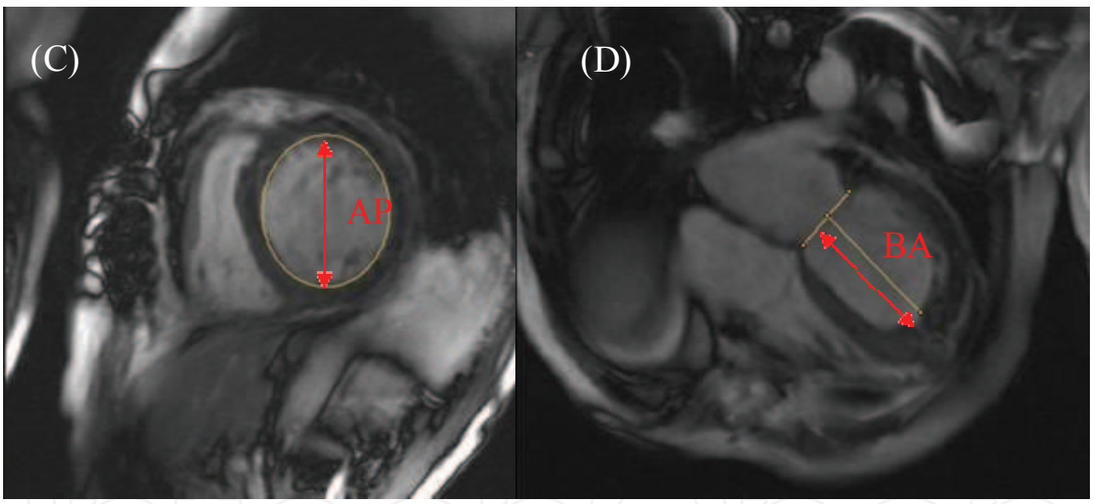


(b) Post-SVR

Fig. 12. Short-axis (panels A and C) and long-axis (panels B and D) magnetic resonance images of patients, before (panels A and B) and after (panels C and D) surgical ventricular restoration (SVR). Multiple short-axis cines from the apex to the base of the heart (or orientated axial) and long-axis cines are used to quantify LV function. Anterior-posterior (AP) (panels A and C) and base-apex (BA) (panels B and D) were measured from 2-D CMR imaging before (panels A and B) and after (panels C and D) SVR during cardiac cycle. The shape factor S, eccentricity index and sphericity index (SI) were calculated from Equation (6). It can be noted that the long-axis decreased more dramatically compared with the short-axis dimension, thereby producing a more spherical ventricle. This figure is adopted from our work presented in Ref 19.

### 7.3 Clinical results

All 40 patients were treated with CABG and SVR (endoventricular circular patch plasty). The age of the patients averaged 69 years (range, 52-84 years). Among them, 19 patients had severe mitral regurgitation and received additional MVS. 28 patients had CHF. The baseline patient characteristics are summarized in Table 8.

| Variables | Value |
|---|---|
| Male : female | 36:4 |
| Age (years) | 69 ± 9 |
| Body surface area ($m^2$) | 1.98 ± 0.18 |
| Coronary artery disease | 39 (98%) |
| Hypertension | 19 (48%) |
| Diabetes mellitus | 13 (33%) |
| Tobacco | 23 (58%) |
| Congestive heart failure | 28 (70%) |
| Peripheral arterial disease | 3 (8%) |
| Stroke | 2 (5%) |
| Creatinine (mg/dL) | 1.17 ± 0.29 |
| Prior cardiac surgery | 19 (48%) |
| New York Heart Association class | |
| I-II | 26 (65%) |
| III-IV | 14 (35%) |
| Surgery | |
| Surgical ventricular restoration + coronary artery bypass grafting | 21 (52%) |
| Surgical ventricular restoration + coronary artery bypass grafting + mitral valve surgery | 19 (48%) |
| Values are mean ± SD or numbers of patients (percentages). | |

Table 8. Patients' characteristics and clinical data (n=40). This table is related to our work in Ref [19].

### 7.4 Left ventricular functional indexes changes pre and post-surgery (MRI parameters)

Figure 12 shows typical short-axis and long-axis magnetic resonance images of patient pre- and post-SVR and how to calculate shape, eccentricity and sphericity index. It is noted that the long-axis decreased more dramatically compared with short-axis dimension, thereby producing a more spherical LV. Figure 13 shows typical 3-dimensional modeling of LV from CMR images using LVtools pre and post SVR.

The intraobserver and interobserver data for EDV, ESV and mass for pre- and post-surgery groups are shown in Table 9. Table 10 summarizes the mean LV functional indexes pre and post-SVR. Following SVR, there was a significant decrease in the dimensions of both the long- and short-axes of the LV. However, the long-axis dimension of the LV decreased more than the short-axis dimension, resulting in a more spherical ventricle post-SVR. There was a significantly reduction in end-diastolic volume index (EDVI), end-systolic volume index (ESVI), LV stroke volume index (SVI), LV mass index, and peak normalized wall stress after

SVR (Table 3). The values of LV EDVI, ESVI, LVEF and the contractility index $d\sigma^*/dt_{max}$ pre- and post-SVR are also shown in the scatter plots of Figure 14.

Table 10 provides the sphericity index (SI) values in end-diastole and end-systole and its diastolic-systolic change, as well as the % shortening of the long- and short-axes. During a cardiac cycle, LV shape becomes less spherical in systole (SI smaller) than in diastole (SI closer to '1'). The diastolic-systolic change in SI ($SI_{ed}$-$SI_{es}$) is significantly augmented by the operation, despite the LV chamber becoming more spherical. The % shortening of long-axis is not significantly altered, but the % shortening of the short-axis is significantly increased by the operation. Despite the seemingly unfavorable spherical LV shape post-SVR, the LV contractile function is significantly improved, as indicated by the increased value of $d\sigma^*/dt_{max}$.

The scatter plots of figure 14 graphically illustrate pre- and post-SVR values of ventricular end-diastolic volume, end-systolic volume, LVEF and contractility index $d\sigma^*/dt_{max}$. From Tables 9 and 10, we can note a significant reduction in end-diastolic volume (318 ± 63 ml vs. 206 ± 59 ml, $p<0.01$), end-systolic volume (228 ± 58 ml vs. 133 ± 61 ml, $p<0.01$), LV mass (204 ± 49 g vs. 187 ± 53 g, $p<0.01$), and peak normalized wall stress (PNWS) (4.64 ± 0.98 vs. 3.72 ± 0.87, $p<0.01$). Increased sphericity index SI (0.57 ± 0.094 vs. 0.67 ± 0.13, $p<0.01$) and increased shape factor (S) (0.44 ± 0.085 vs. 0.54 ± 0.089, $p<0.01$) during end-systole indicates that the LV became more spherical after SVR.

| | Pre-SVR | | | Post-SVR | | |
|---|---|---|---|---|---|---|
| | End diastolic volume (ml) | End systolic volume (ml) | LV mass (g) | End diastolic volume (ml) | End systolic volume (ml) | LV mass (g) |
| Intraobserver | | | | | | |
| Mean | 318 ± 63 | 228 ± 58 | 204 ± 49 | 206 ± 59 | 133 ± 61 | 187 ± 53 |
| Mean difference | 1.1 ± 8.60 | -1.4 ± 8.38 | -5.1 ± 7.96 | 0.3 ± 6.94 | -1.5 ± 3.20 | 0.6 ± 8.51 |
| Correlation coefficient | 0.99 | 0.99 | 0.99 | 0.99 | 0.99 | 0.99 |
| t-test p | N.S. | N.S. | N.S. | N.S. | N.S. | N.S. |
| % variability | 1.50 ± 1.99 | 2.13 ± 2.45 | 3.74 ± 3.71 | 2.42 ± 2.32 | 1.79 ± 1.77 | 4.09 ± 3.02 |
| Interobserver | | | | | | |
| Mean | 318 ± 65 | 231 ± 61 | 206 ± 52 | 207 ± 60 | 135 ± 62 | 189 ± 51 |
| Mean difference | 0.3 ± 10 | 7.9 ± 10 | 7.6 ± 14 | 2.0 ± 8.9 | 5.5 ± 10 | 3.1 ± 9.8 |
| Correlation coefficient | 0.99 | 0.99 | 0.97 | 0.99 | 0.99 | 0.98 |
| t-test p | N.S. | N.S. | N.S. | N.S. | N.S. | N.S. |
| % variability | 2.73 ± 1.58 | 4.11 ± 2.93 | 5.90 ± 3.13 | 3.44 ± 2.94 | 5.87 ± 6.23 | 4.81 ± 2.49 |
| N.S., not significant.<br>Data are mean ± SD. | | | | | | |

Table 9. Reproducibility data in patients pre- and post-SVR. This table is related to our work in Ref [19].

The prime effect of SVR may be viewed as: (i) effecting a decrease in myocardial oxygen consumption by reduction of LV peak normalized wall stress, resulting in improved functioning of LV, and (ii) augmentation of value of the contractility index $d\sigma^*/dt_{max}$ (2.69 ± 0.74 $s^{-1}$ vs. 3.23 ± 0.73 $s^{-1}$, $p<0.01$). This improvement may be attributed to (i) increased maximal flow $dV/dt_{max}$ with reduced LV mass, and (ii) improved regional contraction and contractility of the remote myocardium. The improvement in remote myocardial performance is likely due to reduced myocardial stress, along with effective and complete revascularization. This is because the SVR procedure reduces the volume by more dramatically reducing long-axis dimension compared with the short-axis dimension, and producing a more spherical ventricle.

Based on Table 10, increased LV contractile function $d\sigma^*/dt_{max}$ can be not only associated with increased maximal flow $dV/dt_{max}$, reduced LV mass, and also increased maximal change rate of shape factor $dS/dt_{max}$ ($r=0.414$, $p<0.001$). There was also good correlation between $d\sigma^*/dt_{max}$ and LVEF ($r=0.69$, $p<0.001$, pre-SVR; $r=0.77$, $p<0.001$, post-SVR) (Figure 15).

| Variables | Pre SVR (n=40) | Post SVR (n=40) |
|---|---|---|
| Cardiac index (L/min/$m^2$) | 2.84 ± 0.74 | 2.59 ± 0.74 |
| Mean arterial pressure (mmHg) | 85 ± 14 | 84 ± 8 |
| Systolic blood pressure (mmHg) | 115 ± 20 | 113 ± 10 |
| Diastolic blood pressure (mmHg) | 71 ± 12 | 70 ± 8 |
| End diastolic volume index (ml/$m^2$) | 156 ± 39 | 110 ± 33* |
| End systolic volume index (ml/ $m^2$) | 117 ± 39 | 77 ± 31* |
| Stroke volume index (ml/ $m^2$) | 39 ± 9 | 33 ± 8* |
| Left ventricular ejection fraction (%) | 26 ± 7 | 31 ± 10* |
| LV mass index (g/$m^2$) | 112 ± 25 | 101 ± 23* |
| End-diastolic long axis, $BA_{ed}$(cm) | 10.89 ± 1.16 | 8.31 ± 1.00* |
| End-diastolic short axis, $AP_{ed}$(cm) | 7.00 ± 0.80 | 6.64 ± 0.78* |
| End-systolic long axis, $BA_{es}$(cm) | 10.37 ± 1.20 | 7.87 ± 1.05* |
| End-systolic short axis, $AP_{es}$ (cm) | 5.86 ± 0.98 | 5.23 ± 1.06* |
| End-diastolic sphericity Index, $SI_{ed}$ | 0.65 ± 0.087 | 0.81 ± 0.11* |
| End-systolic sphericity index, $SI_{es}$ | 0.57 ± 0.094 | 0.67 ± 0.13* |
| Difference between end-diastolic and end-systolic sphericity index, $SI_{ed}$ - $SI_{es}$ | 0.077 ± 0.043 | 0.14 ± 0.059* |
| Long axis shortening (%) | 4.8 ± 3.6 | 5.4 ± 4.4 |
| Short axis shortening (%) | 16.4 ± 6.8 | 22 ± 9.7* |
| $dV/dt_{max}$ (ml/s) | 364 ± 83 | 401 ± 81* |
| Pressure normalized wall stress | 4.30 ± 0.95 | 3.31 ± 0.75* |
| Stroke work (mmHg·L) | 6.61 ± 1.96 | 5.46 ± 1.64* |
| $d\sigma^*/dt_{max}$ ($s^{-1}$) | 2.69 ± 0.74 | 3.23 ± 0.73* |

*$p < 0.05$.
Values are mean ± SD.

Table 10. Patients' data pre- and post-SVR. This table is related to our work in Ref [19].

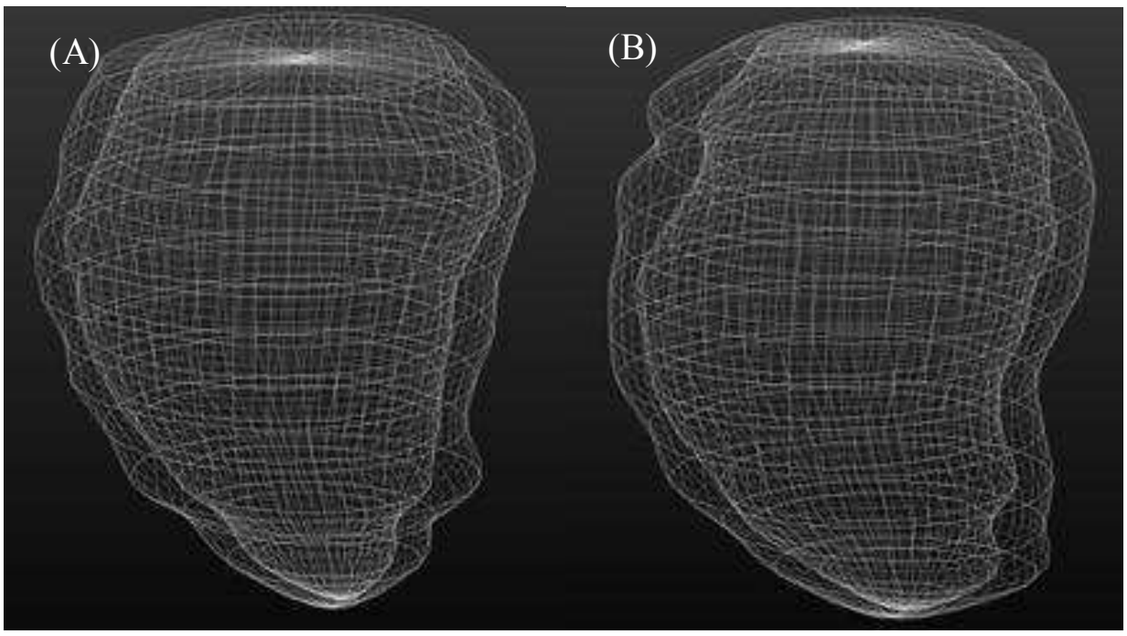


(a)Pre-SVR ED & ES

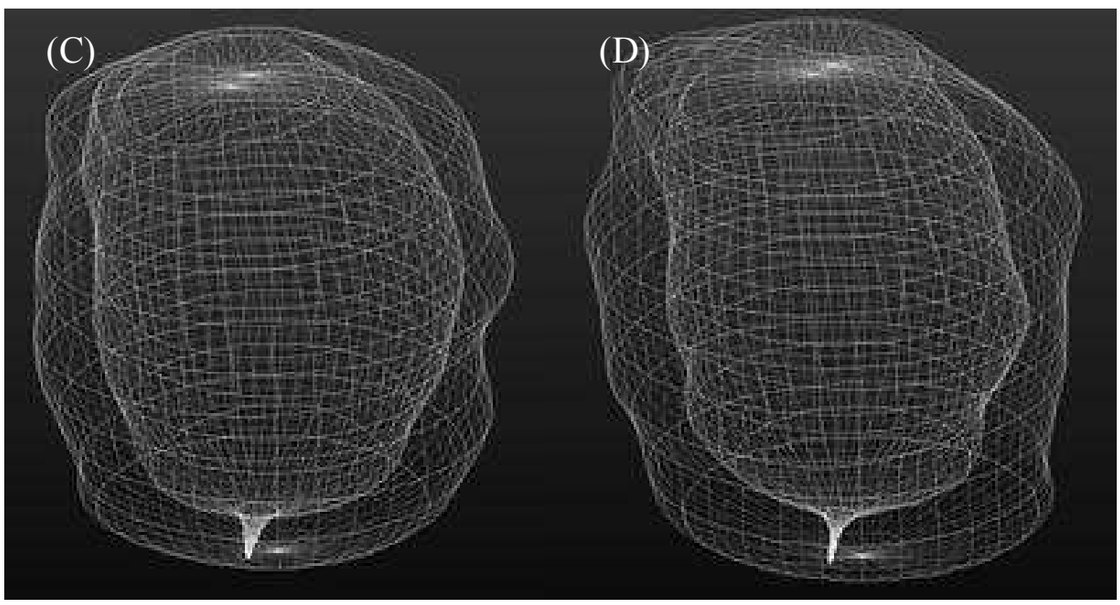


(b) Post-SVR ED & ES

Fig. 13. 3-dimensional reconstructions during end-diastole (panels A and C) and end-systole (panels B and D) phases before (panels A and B) and after (panels C and D) SVR using LVtools. It is created from the endocardial and epicardial contours, which were drawn for calculations of ventricular volumes and function from the multiple short-axis cines (Figure 12). This figure is based on our work presented in Ref. 19.

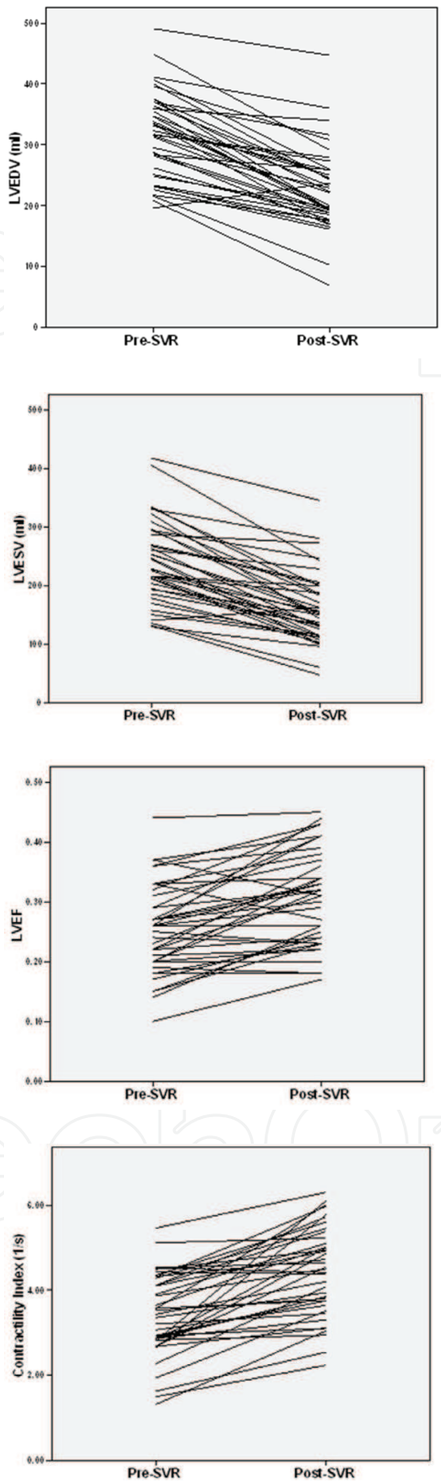


Fig. 14. Changes in end-diastolic volume (EDV), end-systolic volume (ESV), LVEF and contractility index $d\sigma^*/dtmax$ after SVR. This figure is adopted from our work in Ref. 19.

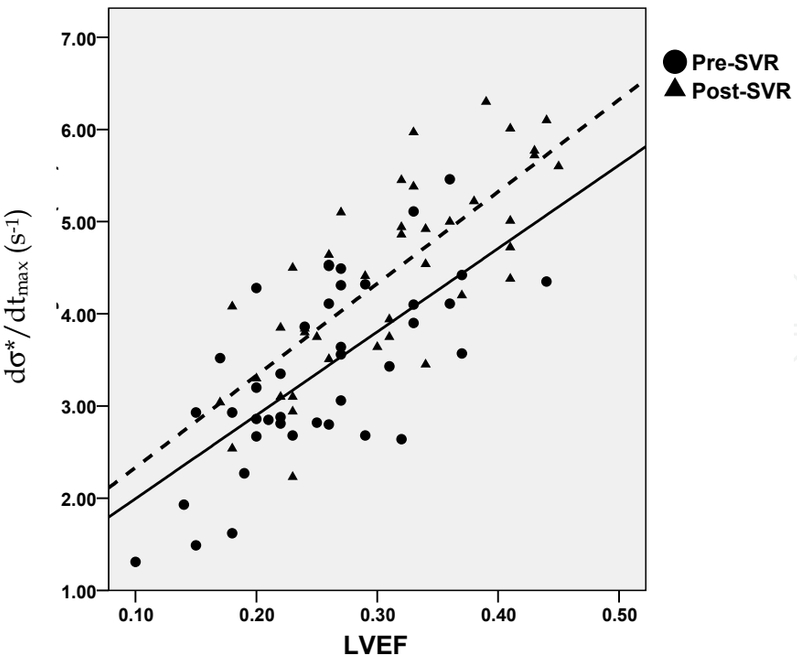


Fig. 15. Association between $d\sigma^*/dt_{max}$ and left ventricular (LV) ejection fraction (EF) pre- and post-SVR. (Solid line: $d\sigma^*/dt_{max}$=9.045×EF+1.091, r=0.69, p<0.001 for pre-SVR; dash line: $d\sigma^*/dt_{max}$=9.969×EF+1.337, r=0.77, p<0.001 for post-SVR). This figure is adopted from our work in Ref 19.

## 8. Conclusion

Myocardial infarct patients' hearts undergo substantial remodeling and loss of contractility, and can progress to heart failure. Echocardiographic texture analysis enables us to determine the percentage volume of the infarcted segments in the ventricular volume.

The ventricular remodelling is defined in terms of reduced alteration in curvedness index (%ΔC) from end-diastole to end-systole. The cardiac contractility is assessed in terms of the value of the index $d\sigma^*/dt_{max}$.

With the help of these three indices of percentage volume of MI segments, curvedness index and contractility index, we can track and assess LV progression to heart failure, and its recovery following CABG and SVR.

## 9. References

[1] Detection of myocardial scars in neonatal infants form computerised echocardiographic texture analysis, by M.V Kamath, R.C Way, D.N. Ghista, T.M. Srinivasan, C. Wu, S Smeenk, C. Manning, J. Cannon, *Engineering in Medicine*, Vol. 15, Vo.3, 1986

[2] A Geometrical Approach for Evaluating Left Ventricular Remodeling in Myocardial Infarct Patients,Yi Su, Liang Zhong, Chi-Wan Lim, Dhanjoo Ghista, Terrance Chua, Ru-San Tan, *Computer Methods and Programs in Biomedicine,* In Press, 2011

[3] Zhong L, Tan RS, Ghista DN, Ng EYK, Chua LP, Kassab GS (2007), Validation of a novel noninvasive cardiac index of left ventricular contractility in patients. *Am J Physiol Heart CircPhysiol,* 292(6):H2764-H2772.

[4] Zhong L, Ghista DN, Ng EYK, Lim ST.Passive and active ventricular elastances of the left ventricle. Biomed Eng Online4: 10, 2005.
[5] Shishido T, Hayashi K, Shigemi K, Sato T, Sugimachi M, Sunagawa K. Single-beat estimation of end-systolic elastance using bilinearly approximated time-varying elastance. *Circulation* 102: 1983–1989, 2000.
[6] Liang Zhong, Kian-Keong Poh, Li-Ching Lee, Thu-Thao Le, Ru-San Tan, Attenuation of Stress-based Ventricular Contractility in Patients with Heart Failure and Normal Ejection Fraction,Annals, Academy of Medicine, Singapore, April 2011, Vol 40, No 4
[7] Hogg K, Swedberg K, McMurray J. Heart failure with preserved left ventricular systolic function: epidemiology, clinical characteristics, and prognosis. *J Am Coll Cardiol.*2004;43:317-327.
[8] Little WC. The left ventricular (dP/dt)max-end-diastolic volume relation in closed-chest dogs. *Circ Res.* 1985;56:808-815.
[9] Vasan RS, Levy D. Defining diastolic heart failure: a call for standardized diagnostic criteria. *Circulation*. 2000;101:2118-2121.
[10] Devereux RB, Alonso DR, Lutas EM, Gottlieb GJ, Campo E, Sachs I, Reichek N. Echocardiographic assessment of left ventricular hypertrophy: comparison to necropsy findings. *Am J Cardiol*. 1986;57:450-458.
[11] Lang RM, Bierig M, Devereux RB, Flachskampf FA, Foster E. Recommendations for chamber quantification. *J Am SocEchocardiogr*. 2005;18:1440-1463.
[12] Kitzman DW, Gardin JM, Gottdiener JS, et al. Importance of heart failure with preserved systolic function in patients > or =65 years of age. CHS Research Group Cardiovascular Health Study. *Am J Cardiol*. 2001;87:413-419.
[13] Banerjee P, Banerjee T, Khand A, et al. Diastolic heart failure: neglected or misdiagnosed? *J Am CollCardiol*. 2002;39:138-141.
[14] Burkhoff D, Maurer MS, Packer M. Heart failure with a normal ejection fraction: is it really a disorder of diastolic function? *Circulation*. 2003;107:656-658
[15] Zhang, J.M., Chua, L.P., Ghista, D.N., Yu, S.C.M. and Tan, Y.S., Numerical investigation and identification of susceptible site of atherosclerotic lesion formation in a complete coronary artery bypass model, *J. of Medical and Biological Engineering and Computing*, 2008, Vol. 46 (7), pp. 689-699.
[16] Sankaranarayanan, M., Chua L. P., Ghista D. N. and Tan Y. S., Computational model of blood flow in the aorta-coronary bypass graft, *BioMedical Engineering Online,*2005,4:14.
[17] Chua, L.P., Zhang, J.M., Yu, S.C.M., Ghista, D.N. and Tan, Y.S., Numerical study on the pulsatile flow characteristics of proximal anastomotic model, *J. of Engg. in Medicine, Proceedings of the Institution of Mechanical Engineers Part H,* 2005, Vol. 219, pp 361-379.
[18] Xiong, F.L., and Chong, C.K., A parametric numerical investigation on haemodynamics in distal coronary anastomoses, *Medical Engineering and Physics*, 2008, Vol. 30(3), pp. 311-320.
[19] Zhong L, Sola S, Tan RS, Ghista DN, Kurra V, Navia JL, Kassab GS. Effects of surgical ventricular restoration on left ventricular contractility assessed by a novel contractility index in patients with ischemic cardiomyopathy. *Am J Cardiol* 103: 674-679, 2009.
[20] Streeter Jr DD, Hanna WT. Engineering mechanics for successive states in canine left ventricular myocardium. I Cavity and wall geometry.*Circ Res*. 1973;33:639-655.
[21] Dhanjoo N. Ghista, *Applied Biomedical Engineering,* CRC Press, 2009

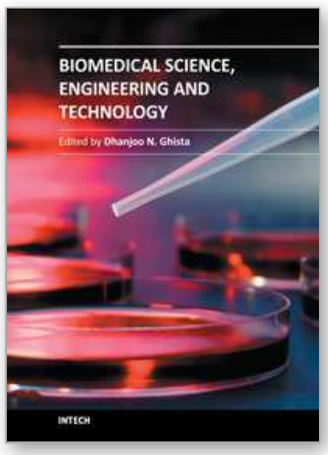


**Biomedical Science, Engineering and Technology**

Edited by Prof. Dhanjoo N. Ghista

ISBN 978-953-307-471-9
Hard cover, 902 pages
**Publisher** InTech
**Published online** 20, January, 2012
**Published in print edition** January, 2012

This innovative book integrates the disciplines of biomedical science, biomedical engineering, biotechnology, physiological engineering, and hospital management technology. Herein, Biomedical science covers topics on disease pathways, models and treatment mechanisms, and the roles of red palm oil and phytomedicinal plants in reducing HIV and diabetes complications by enhancing antioxidant activity. Biomedical engineering coves topics of biomaterials (biodegradable polymers and magnetic nanomaterials), coronary stents, contact lenses, modelling of flows through tubes of varying cross-section, heart rate variability analysis of diabetic neuropathy, and EEG analysis in brain function assessment. Biotechnology covers the topics of hydrophobic interaction chromatography, protein scaffolds engineering, liposomes for construction of vaccines, induced pluripotent stem cells to fix genetic diseases by regenerative approaches, polymeric drug conjugates for improving the efficacy of anticancer drugs, and genetic modification of animals for agricultural use. Physiological engineering deals with mathematical modelling of physiological (cardiac, lung ventilation, glucose regulation) systems and formulation of indices for medical assessment (such as cardiac contractility, lung disease status, and diabetes risk). Finally, Hospital management science and technology involves the application of both biomedical engineering and industrial engineering for cost-effective operation of a hospital.

**How to reference**

In order to correctly reference this scholarly work, feel free to copy and paste the following:

Dhanjoo N. Ghista, Liang Zhong, Leok Poh Chua, Ghassan S. Kassab, Yi Su and Ru San Tan (2012). Cardiac Myocardial Disease States Cause Left Ventricular Remodeling with Decreased Contractility and Lead to Heart Failure;Interventions by Coronary Arterial Bypass Grafting and Surgical Ventricular Restoration Can Reverse LV Remodeling with Improved Cont, Biomedical Science, Engineering and Technology, Prof. Dhanjoo N. Ghista (Ed.), ISBN: 978-953-307-471-9, InTech, Available from: http://www.intechopen.com/books/biomedical-science-engineering-and-technology/cardiac-myocardial-infarction-leading-to-heart-failure-prevented-by-surgical-ventricular-restoration

INTECH
open science | open minds

**InTech Europe**
University Campus STeP Ri
Slavka Krautzeka 83/A
51000 Rijeka, Croatia

**InTech China**
Unit 405, Office Block, Hotel Equatorial Shanghai
No.65, Yan An Road (West), Shanghai, 200040, China
中国上海市延安西路65号上海国际贵都大饭店办公楼405单元

Phone: +385 (51) 770 447
Fax: +385 (51) 686 166
www.intechopen.com

Phone: +86-21-62489820
Fax: +86-21-62489821



IntechOpen

IntechOpen